Thin-Walled Structures 182 (2023) 110165

Contents lists available at ScienceDirect

Thin-Walled Structures

journal homepage: www.elsevier.com/locate/tws

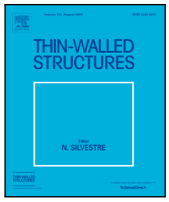

Full length article

Experimental study and numerical simulation on the seismic behavior of diagonally stiffened stainless steel plate shear walls under low cyclic loading

Yiwen Wu [a], Shenggang Fan [a,*], Yang Guo [b], Shengjie Duan [a], Qixun Wu [a]

[a] Key Laboratory of Concrete and Prestressed Concrete Structures of Ministry of Education, School of Civil Engineering, Southeast University, Jiulonghu Campus, Nanjing 211189, China
[b] ARTS Group Co., Limited, Suzhou, 215124, China

ARTICLE INFO

Keywords:
Stainless steel
Steel plate shear wall
Seismic behavior
Low cyclic loading

ABSTRACT

To expand the application scope of stainless steel, especially in the seismic resistance, a series of systematic studies from material to members were carried out. A mechanical property test of S30408 austenitic stainless steel under monotonic loading and cyclic loading was conducted first. Then, a low cyclic loading test of 8 diagonally stiffened steel plate shear walls (SPSWs), including 6 stainless SPSWs, 1 LY100 low-yield-strength SPSW and 1 Q235 SPSW, was carried out. The failure modes, hysteresis curves, skeleton curves, ductility coefficient and equivalent viscous damping ratio-displacement angle curves of different SPSWs were compared. The mechanical behavior, energy dissipation and failure mechanism were revealed. The test results showed that the ductility of stainless SPSWs was the greatest. An effective tension field was formed after buckling. Even if the displacement angle exceeded 1/50, a good bearing capacity was displayed. A corner tearing for the LY100 and Q235 SPSWs occurred in the late stage of loading, resulting in a failure to form a reliable tension field. A notable decline in bearing capacity occurred, and the ductility was poor. The energy dissipation of the stainless SPSWs was better than that of the Q235 SPSW but slightly worse than that of the LY100 SPSW. Considering the limitation of the test, such as the limitation of the specimen number and the range of the investigation parameters, a refined finite element model was established and a parametric analysis was conducted, mainly considering the influence of aspect ratio α, height-thickness ratio λ, stiffness ratio of periphery stiffener η_f and stiffness ratio of diagonal stiffener η_s on the hysteretic performance. The research carried out herein offers a reliable reference for this new lateral force resisting structure and provides data for subsequent research, which is helpful to promote the application of stainless SPSWs in building structures.

1. Introduction

In recent years, with the rapid development of various building structures, the demand for new construction materials is increasing. Stainless steel, a new construction material, has many advantages such as high strength, light weight and superior appearance. Moreover, a short service life of the anticorrosive measures commonly used in engineering appears, and many human and financial resources need to be invested in later maintenance, resulting in high costs. However, stainless steel can fundamentally solve this problem from the material aspect [1]. More importantly, excellent ductility and energy dissipation make stainless steel be a good seismic material. Nevertheless, existing research on the seismic behavior of stainless steel is rare. Besides, among the stiffeners in all directions, small magnitude of corrugation of diagonal stiffeners in plates will exhibit much superior strength and stiffness. Diagonal stiffeners can also effectively limit the out-of-plane buckling of thin steel plates to improve the stiffness and energy consumption capacity [2–6].

At present, research on stainless steel mostly focuses on the material mechanical properties and the static bearing capacity of members under monotonic loading. Many scholars have proposed a series of mature stainless steel constitutive models [7–10]. Regarding the static bearing capacity of stainless steel members, Rasmussen [11–14] conducted many studies on the bearing capacity of stainless steel compression members. Additionally, Rossi [15], Zheng [16] and Zhao [17] studied different types of stainless steel compression members, while Huang [18], Hassanein [19], Niu [20,21], and Fan [22,23] studied stainless steel flexural members.

Although many codes [24–26] have given design formulas for stainless steel materials and members, there is a lack of research on the seismic behavior of stainless steel. A constitutive model of stainless steel under cyclic loading is the basis for structure elastoplasticity seismic analysis. However, due to complex test equipment and difficult operation, test results usually fail to meet expectations, and research is rare [27–29]. Moreover, research on stainless SPSWs is lacking. Since

* Corresponding author.
E-mail address: 101010393@seu.edu.cn (S. Fan).

https://doi.org/10.1016/j.tws.2022.110165
Received 24 April 2022; Received in revised form 9 September 2022; Accepted 15 September 2022
Available online xxxx
0263-8231/'

the 1970s, many scholars have carried out many studies on SPSWs, but most of them focus on standard or low-yield-strength SPSWs. Takahashi et al. [30] conducted an in-depth experimental research and theoretical analysis on standard SPSWs for the first time. The test specimens were 12 one-story one-bay and 2 one-story two-bay hinged frames with stiffened SPSWs. The test results showed that the hysteresis curves of the nonstiffened SPSWs were shuttle shaped, the pinching was significant, and an elastic–plastic yield occurred for most specimens. Good hysteresis behavior, no pinching and good ductility appeared for the stiffened SPSWs. Subsequently, Takahashi held a point that the stiffness and yield strength of stiffened SPSWs could be calculated by shear theory through a finite element analysis and suggested that elastic buckling should be taken as the design criterion for stiffened SPSWs. Xue and Lu [31,32] conducted experimental research on 4 twelve-story three-bay thin SPSWs. The test results showed that an additional axial force and moment displayed for SPSWs connected at four sides led to a premature failure of the side columns. SPSWs connected at both sides could avoid the premature failure of side columns, but the lateral stiffness was lower. Azandariani [33] carried out an experimental and numerical investigation of the cyclic behavior of low-yield-strength SPSWs. The results indicated good stiffness, high ductility, significant energy dissipation, and stable cyclic behavior for the test specimens. The type of beam-to-column connection affected ductility, strength and energy dissipation and had a negligible effect on the initial stiffness. Nakashima and Torii et al. [34–37] studied the seismic performance of low-yield-strength SPSWs in high-rise buildings. The results showed an earlier yield, superior ductility, outstanding energy dissipation and stable hysteresis loop for low-yield-strength SPSWs. Compared with standard SPSWs, low-yield-strength SPSWs had better energy dissipation and longer low cyclic fatigue life.

Overall, at present, there are many studies and applications on standard and low-yield-strength SPSWs, while limited research has been conducted on the seismic behavior of stainless SPSWs. Therefore, a mechanical property test of S30408 austenitic stainless steel under monotonic loading and cyclic loading was conducted first. Then, a low cyclic loading test of 6 diagonally stiffened stainless SPSWs was carried out. In addition, 1 LY100 low-yield-strength SPSW and 1 Q235 SPSW test were conducted for comparison. A further parametric analysis was conducted to investigate influence of aspect ratio α, height-thickness λ, stiffness ratio of periphery stiffener η_f and stiffness ratio of diagonal stiffener η_s on the hysteretic performance. The research carried out herein makes up for the blank of stainless SPSWs and further promotes the application of stainless steel in the construction.

2. Material mechanical property tests under monotonic and cyclic loading

Material mechanical properties are the basis of seismic analysis of structures and members and provide data for subsequent numerical simulation. Therefore, a mechanical property test under monotonic and cyclic loading was carried out for the same batch of materials of subsequent SPSWs.

2.1. Mechanical property test under monotonic loading

Three kinds of materials, S30408 austenitic stainless steel, LY100 low-yield-strength steel and Q235 steel, were tested in the mechanical property test under monotonic loading. The thicknesses of stainless steel were 2.0 mm, 2.5 mm and 3.0 mm, and the thickness of LY100 low-yield-strength steel and Q235 steel was 3.0 mm.

2.1.1. Specimen dimension under monotonic loading

According to GB/T 228.1-2010 Metallic Materials-Tensile Testing at Room Temperature [38], the dimensions of the specimens are shown in Fig. 1. Where, t is the thickness of the specimens.

According to different materials and thicknesses, the test specimens were divided into 5 groups, with 3 specimens in each group. Groups and codes of the test specimens are shown in Tables 1 and 2.

2.1.2. Loading method under monotonic loading

According to GB/T 228.1-2010 Metallic Materials-Tensile Testing at Room Temperature [38], using a CMT5105 electronic universal test machine, tensile loading was conducted in two stages: (1) In the first stage, the specimen was stretched to 0.02 strain at a rate of 0.5 mm/min to obtain the initial elastic modulus and nominal yield strength. (2) In the second stage, the specimen was stretched to failure at a rate of 5 mm/min to obtain the ultimate tensile strength.

2.1.3. Test results under monotonic loading

$$\varepsilon = \begin{cases} \dfrac{\sigma}{E_0} + 0.002\left(\dfrac{\sigma}{\sigma_{0.2}}\right)^n & 0 \le \sigma \le \sigma_{0.2} \\ \dfrac{\sigma-\sigma_{0.2}}{E_{0.2}} + \varepsilon_u\left(\dfrac{\sigma-\sigma_{0.2}}{\sigma_u-\sigma_{0.2}}\right)^m + \varepsilon_{0.2} & \sigma_{0.2} < \sigma \le \sigma_u \end{cases} \quad (1)$$

$$\delta_u = \frac{L_u - L_0}{L_0} \times 100\% \quad (2)$$

where, L_u is the standard distance after failure; L_0 is the initial standard distance.

Referring to the stainless steel constitutive model proposed by Rasmussen [10], the mechanical property parameters of each specimen can be obtained, as shown in Table 1. The mechanical property parameters of Q235 steel and LY100 steel are shown in Table 2, and the yield ratio and elongation of Q235 steel can meet the requirements in GB 50017-2017 Standard for Design of Steel Structures [39]. The meaning and calculation method of each parameter are in the table note.

2.2. Mechanical property test under cyclic loading

In the mechanical property test under cyclic loading, to prevent the specimens from buckling, the thickness should be as large as possible. Therefore, the thickness of all test specimens was 3.0 mm.

2.2.1. Specimen and clamp design

According to GB/T 26077-2010 Metallic Materials-Fatigue Testing-Axial-Strain-Controlled Method [40], the cyclic loading test specimen dimensions are shown in Fig. 2.

To prevent compression bending instability of thin plates under cyclic loading, referring to Ref. [40–42], an anti-bending clamp suitable for the mechanical property test of stainless steel under cyclic loading was designed. The plane dimension and 3D diagram of the clamp are shown in Fig. 3(a) and (b). Fig. 3(b) shows that the upper and lower ends of the specimens were connected with the test machine through the clamping end, and two I-shaped clamps were connected by ordinary bolts. The clamp was made of 304 austenitic stainless steel, and the surface was polished to reduce the friction between the clamp and the specimen as well as the impact on the test force. Ref. [41] showed that the influence of a certain clamping force applied to the anti-bending device on the test force could be ignored.

2.2.2. Loading method under cyclic loading

Referring to the cyclic loading tests carried out in Refs. [27–29,43], four loading methods were designed, and a triangular wave was adopted. Specimen C0 was loaded monotonically and the loading method was the same as that of the monotonic loading test above. Specimens C1-1 and C1-2 were loaded symmetrically with equal amplitudes, and the strain amplitudes were 1.25% and 2.5%, respectively. Each was loaded 20 times, and the loading rate was 0.001/s. Specimen C2 was loaded with variable amplitude and loaded symmetrically step by step with equal strain increments of 0.25%. Specimen C2 was pulled first and then pressed and loaded 10 times with a loading rate of 0.001/s. Loading curves of Specimens C1-1~C2 are shown in Fig. 4.

Table 1
Groups, codes and mechanical properties of stainless steel specimens.

Group	Code	E_0/MPa	$\sigma_{0.2}$/MPa	σ_u/MPa	$\varepsilon_{0.2}$/%	ε_u/%	n	m	δ_u
1	S-2.0-1	176 668	261.18	829.27	0.349	68.50	9.84	2.01	62.69%
	S-2.0-2	185 553	265.96	797.83	0.344	66.66	8.70	2.07	61.89%
	S-2.0-3	193 969	252.18	789.15	0.331	68.04	8.66	2.02	62.89%
	Average	185 397	259.77	805.42	0.341	67.73	9.07	2.03	62.49%
2	S-2.5-1	180 282	245.69	767.85	0.337	67.58	8.68	2.02	59.23%
	S-2.5-2	193 085	252.13	767.86	0.330	67.16	10.04	2.08	56.93%
	S-2.5-3	203 529	248.47	766.21	0.323	67.57	9.59	2.00	60.48%
	Average	192 299	248.76	767.31	0.330	67.44	9.44	2.03	58.88%
3	S-3.0-1	181 578	268.85	710.25	0.347	52.61	17.53	2.45	63.00%
	S-3.0-2	186 119	248.61	715.21	0.334	55.29	8.38	2.37	61.08%
	S-3.0-3	203 092	250.87	712.47	0.320	57.15	7.44	2.20	57.88%
	Average	194 606	249.74	712.64	0.327	56.22	7.91	2.29	60.65%

Note: 1. S-t-a: S refers to S30408 austenitic stainless steel; t is the specimen thickness; a is the specimen code.
2. E_0 is the initial elastic modulus. $\sigma_{0.2}$ is the nominal yield strength, that is, the stress corresponding to the residual deformation of 0.2%. $\varepsilon_{0.2}$ is the total stress corresponding to $\sigma_{0.2}$. σ_u is the ultimate tensile strength. ε_u is the ultimate strain. n and m are the strain hardening indexes fitted by Eq. (1). δ_u is the elongation calculated by Eq. (2).

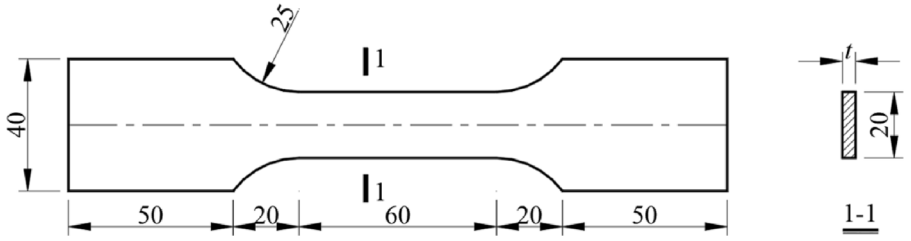

Fig. 1. Specimen dimensions under monotonic loading.

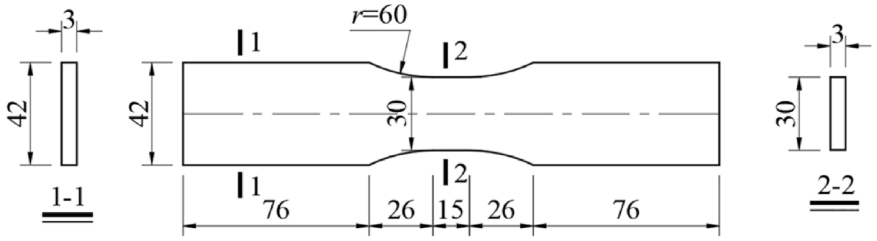

Fig. 2. Specimen dimensions under cyclic loading.

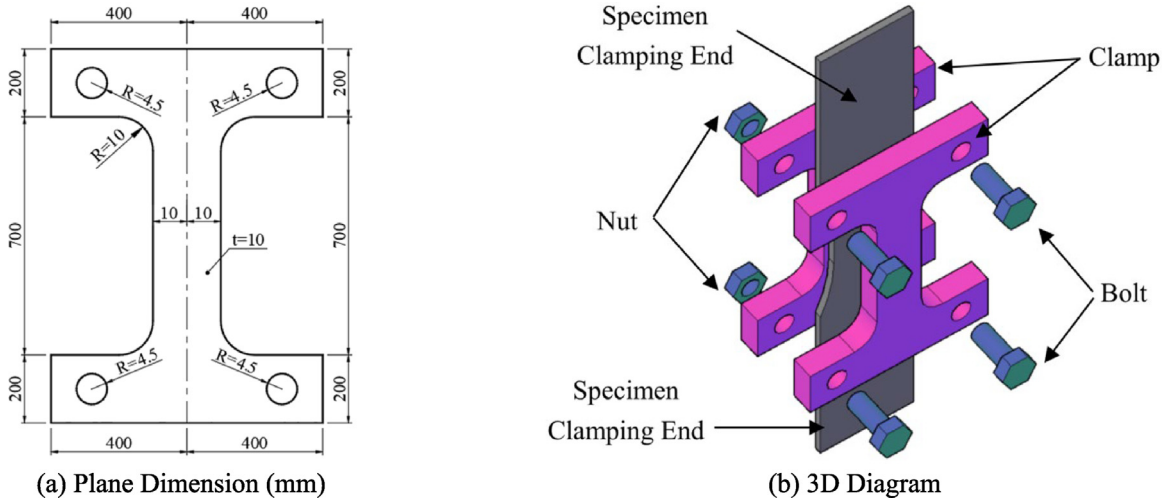

Fig. 3. Anti-bending clamp.

2.2.3. Test phenomena under cyclic loading

The comparison of each specimen before and after the tests is shown in Fig. 5. Fig. 5 shows that (1) in the cyclic loading test, no buckling of the specimens occurs, indicating that the anti-bending clamp has an excellent effect. (2) According to the comparison of test specimens C0, C1-1 and C1-2, the elongation of the test specimens decreases in

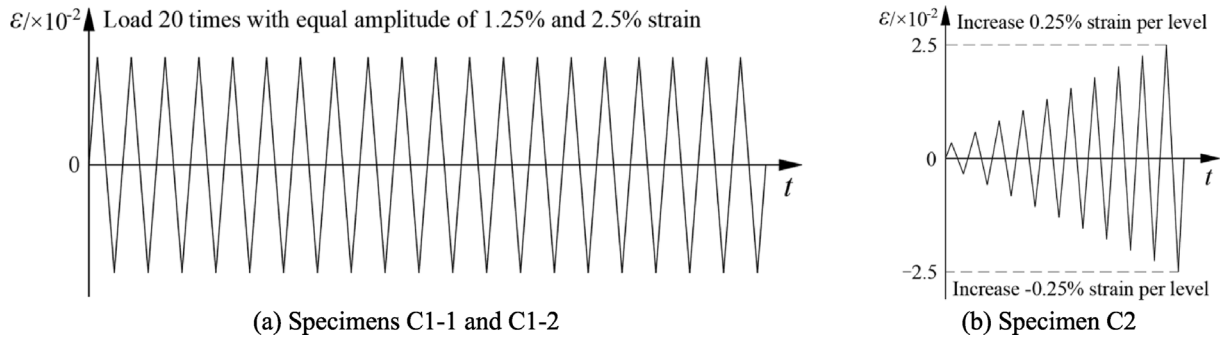

Fig. 4. Loading curves of cyclic loading.

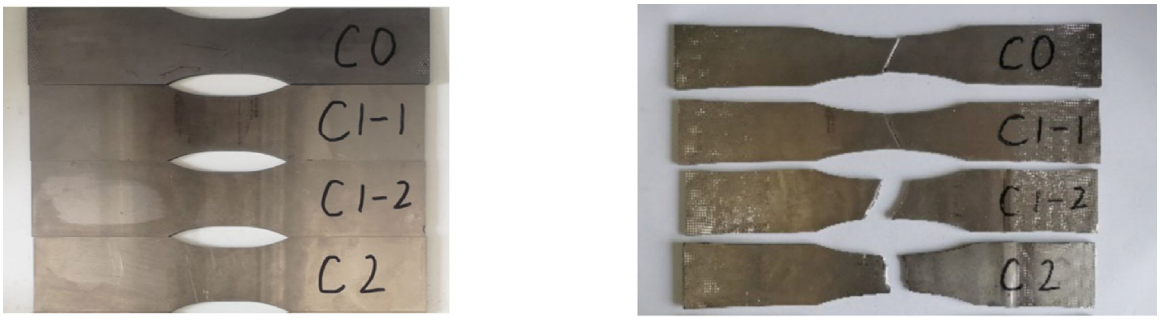

Fig. 5. Comparison of each specimen before and after the tests.

Table 2
Groups, codes and mechanical properties of LY100 low-yield-strength steel and Q235 steel specimens.

Group	Code	E/MPa	f_y/MPa	f_u/MPa	f_y/f_u	δ_u
4	Q-3-1	173 662	265.78	382.37	0.70	41.00%
	Q-3-2	198 095	272.74	382.42	0.71	40.33%
	Q-3-3	211 932	275.80	380.59	0.72	39.04%
	Average	194 563	271.44	381.79	0.71	40.12%
5	L-3-1	181 588	122.37	278.89	0.44	58.89%
	L-3-2	195 925	123.15	279.21	0.44	58.96%
	L-3-3	209 004	117.40	279.69	0.42	61.36%
	Average	195 506	120.97	279.26	0.43	59.74%

Note: 1. Q (L)-t-a: Q refers to Q235 steel; L refers to LY100 low-yield-strength steel; t is the material thickness; a is the specimen code.
2. E is the elastic modulus. f_y is the yield strength. f_u is the ultimate tensile strength. δ_u is the elongation calculated by Eq. (2).

turn, indicating that the ductility of the test specimens under cyclic loading is worse. With increasing loading amplitude, the ductility is worse. (3) According to the comparison of test specimens C1-2 and C2, the elongation of the test specimens is nearly the same, indicating that under the same maximum loading amplitude, the effect of variable and equal loading amplitudes on the ductility of the test specimens is the same.

2.2.4. Test results under cyclic loading

The stress–strain curves of each specimen are shown in Fig. 6. Fig. 6 shows that the hysteresis curves of specimens C1-1, C1-2 and C2 are plump, indicating that the stainless steel material has a good energy dissipation capacity. In addition, the cyclic strengthening of specimens C1-1, C1-2 and C2 is significant, which shows that the hysteretic behavior of stainless steel combines the characteristics of isotropic strengthening and kinematic hardening.

For stainless steel materials, due to different loading methods, there are great differences between the skeleton curve under cyclic loading and the stress–strain curve under monotonic loading. To facilitate the comparison with the stress–strain curve under monotonic load, taking specimen C2 as an example, the skeleton curve of specimen C2 is calculated by Eq. (4). Eq. (4) is modified from Eq. (3) [7].

$$\frac{\Delta\varepsilon}{2} = \frac{\Delta\varepsilon_e}{2} + \frac{\Delta\varepsilon_p}{2} = \frac{\Delta\sigma}{2E} + \left(\frac{\Delta\sigma}{2K'}\right)^{\frac{1}{n'}} \tag{3}$$

$$\varepsilon = \frac{\sigma}{E} + \left(\frac{\sigma}{K'}\right)^{\frac{1}{n'}} \tag{4}$$

where, $\Delta\varepsilon$ is the total strain amplitude; $\Delta\varepsilon_e$ is the elastic strain amplitude; $\Delta\varepsilon_p$ is the plastic strain amplitude; $\Delta\sigma$ is the stable stress amplitude; E is the elastic modulus of stainless steel; K' is the cyclic strengthening coefficient; n' is the cyclic strain hardening index.

According to the characteristic points of the skeleton curve of specimen C2 obtained from the test, it can be determined that $K' = 1594.1$ and $n' = 0.3204$. The stress–strain curve of specimen C0 under monotonic loading and the cyclic skeleton curve of specimen C2 calculated by Eq. (4) are shown in Fig. 7. Fig. 7 shows that Eq. (4) can accurately simulate the cyclic skeleton curve of S30408 austenitic stainless steel. In the later stage of cyclic loading, cyclic hardening improves the strength of the material, and no cyclic softening occurs.

In the widely used finite element software ABAQUS, a nonlinear kinematic hardening/isotropic strengthening model [44] is provided. The isotropic strengthening can be expressed by Eq. (5), which is a function having the equivalent plastic strain $\bar{\varepsilon}^{pl}$ as the parameter, reflecting the yield surface size σ^0.

$$\sigma^0 = \sigma|_0 + Q_\infty\left[1 - \exp\left(-b_{iso}\bar{\varepsilon}^{pl}\right)\right] \tag{5}$$

where, $\sigma|_0$ is the stress when the equivalent plastic strain is 0; Q_∞ is the maximum variation of yield surface; b_{iso} is the change of yield surface size with plastic strain increasing.

For strongly nonlinear materials such as stainless steel, when the nominal yield strength is taken as the initial yield surface, the model results are quite different from the test. Referring to the research of Nip [45], the stress corresponding to 0.01% plastic strain is taken herein as the initial yield surface.

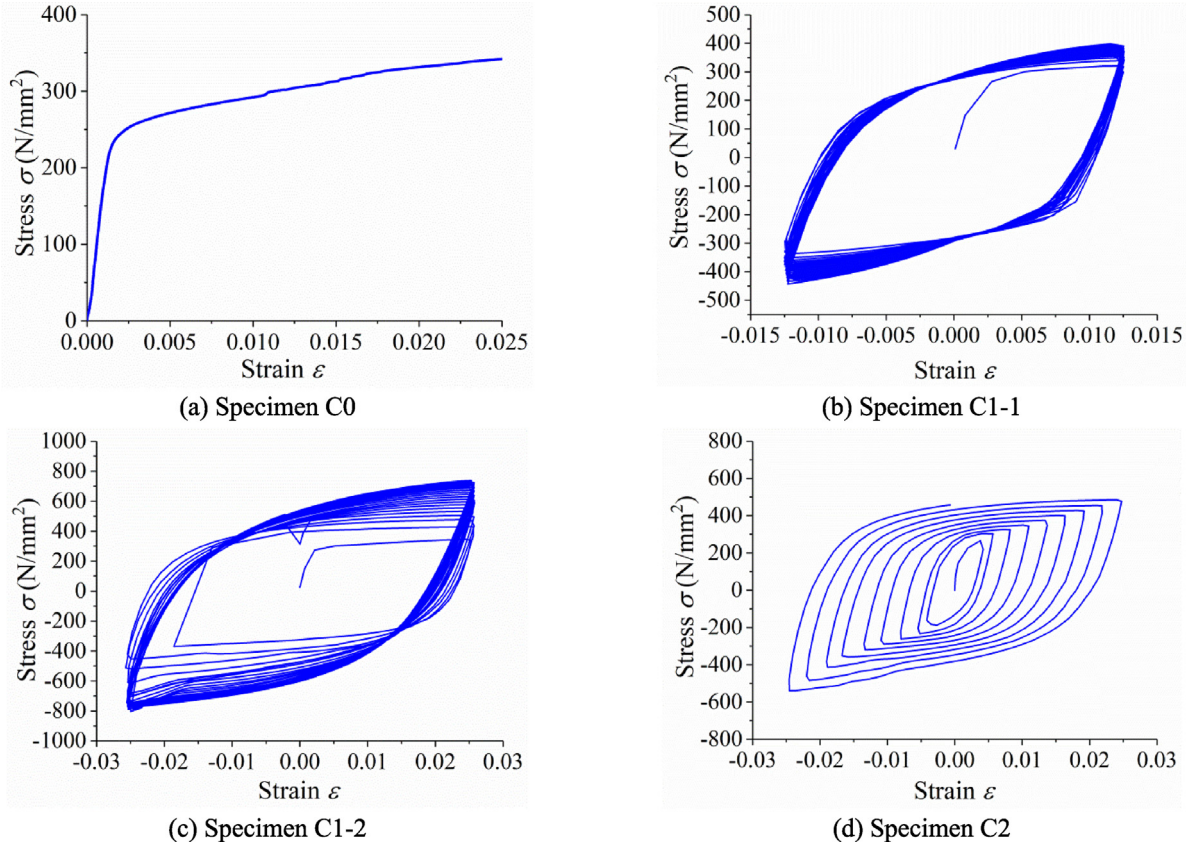

Fig. 6. Stress–strain curves.

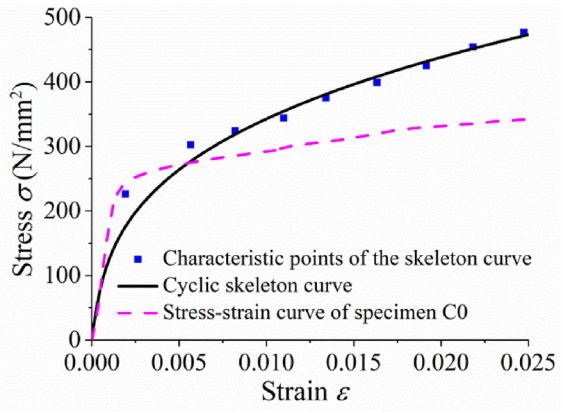

Fig. 7. Comparison between Stress–strain curve of specimen C0 and cyclic skeleton curve of specimen C2.

For the nonlinear kinematic hardening model, the relationship between the back stress α_k and plastic strain ε^{pl} is shown in Eqs. (6) and (7).

$$\alpha_k = \frac{C_{kin,k}}{\gamma_k}\left[1 - \exp\left(-\gamma_k \varepsilon^{pl}\right)\right] + \alpha_{k,1}\exp\left(-\gamma_k \varepsilon^{pl}\right) \tag{6}$$

$$\alpha = \sum_{1}^{N} \alpha_k \tag{7}$$

where, α_k is the kth back stress; $\alpha_{k,1}$ is the kth back stress of the first data; $C_{kin,k}$ and γ_k are the material constant to be calibrated for the kinematic hardening; α is the total back stress.

Based on the test results of stress–strain curves of specimens C1, C2 and C3, the fitted parameters Q_∞, b_{iso}, $C_{kin,k}$ and γ_k are shown in Table 3.

3. Low cyclic loading test of diagonally stiffened stainless SPSWs

To explore the seismic performance of diagonally stiffened stainless SPSWs, a low cyclic loading test on stainless SPSWs was carried out, and the influence of the height-thickness ratio λ, stiffness ratio of diagonal stiffener η_s and material types on seismic performance were investigated. A total of 6 S30408 austenitic stainless SPSWs were designed in the test with 1 LY100 low-yield-strength SPSW and 1 Q235 SPSW for comparison.

3.1. Design of SPSWs

3.1.1. Scale effect

Considering the limitation of test setup, the scale ratio of 1:3 was adopted for the test. The geometry similarity ratio S_L was 1:3. The main parts of SPSWs were made of S30408 austenitic stainless steel, so the material similarity ratio S_E was 1:1. The similarity ratios of various physical quantities in the test are shown in Table 4. Additionally, to apply the test results to the actual full-scale project, in subsequent parametric analysis, the finite element models were designed in full scale.

3.1.2. Construction form

A diagonal stiffened stainless SPSW was designed, as shown in Fig. 8(a). The SPSW was connected on both sides without frame columns either side. To facilitate the connection between the SPSW and the loading device, 22 mm bolt holes were set on the connecting plates

Table 3
Parameter calibration of cyclic constitutive model.

Specimen	$\sigma\|_0$/MPa	Q_∞/MPa	b_{iso}	$C_{kin,1}$/MPa	γ_1	$C_{kin,2}$/MPa	γ_2	$C_{kin,3}$/MPa	γ_3	$C_{kin,4}$/MPa	γ_4
C1	160.14	90	17.5	18 520	440	14 819	109	12 778	129	7728	89
C2	165.54	83	14.2	16 524	333	10 941	61	10 932	61	5914	61
C3	165.92	79	15.1	16 216	422	12 350	70	8416	80	4322	65
Average	164.00	84	15.6	17 087	398	12 703	80	10 709	90	5988	72

Table 4
Similarity ratios of various physical quantities in the test.

Physical quantity	Stress	Strain	Elastic modulus	Poisson's ratio	Length	Displacement	Angle	Concentrated load
Dimension	$[FL^{-2}]$	[1]	$[FL^{-2}]$	[1]	[L]	[L]	[1]	[F]
Similarity ratio relation	S_E	1	S_E	1	S_L	S_L	1	$S_E S_L^2$
Scale ratio	1:1	1:1	1:1	1:1	1:3	1:3	1:3	1:9

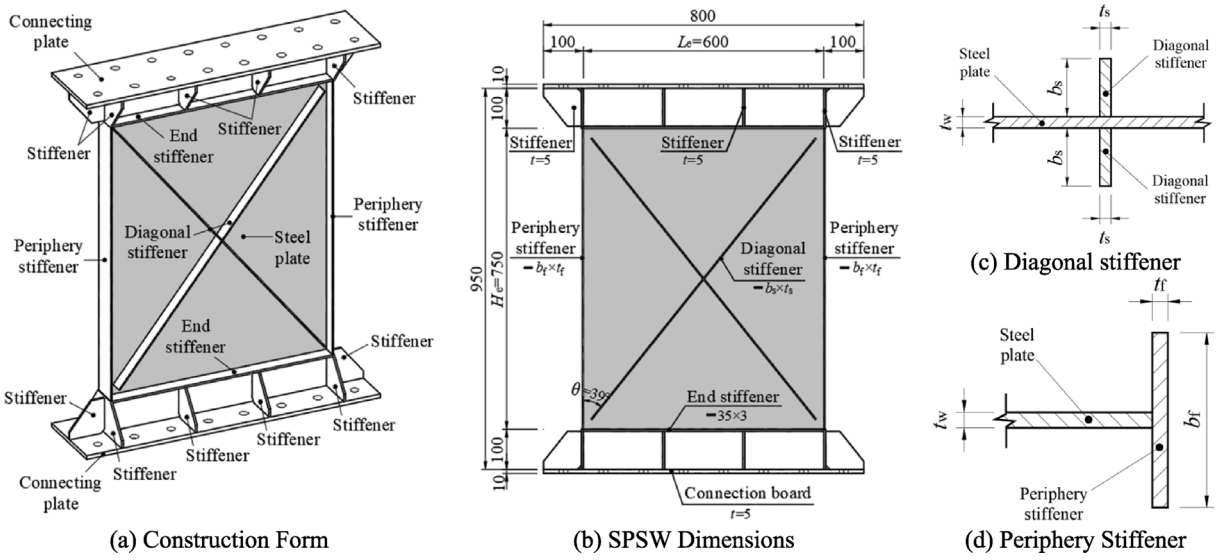

Fig. 8. Construction form and geometric dimensions of SPSWs.

at the upper and lower ends of the SPSW, which were connected with the loading device through M20 high-strength bolts.

In Fig. 8(a): (1) The upper and lower edges of the steel plate were connected with the connecting plate and the upper and lower ends were strengthened with stiffeners. (2) Periphery stiffeners were set to prevent buckling on the left and right sides of the steel plate. (3) For the diagonally stiffened stainless SPSWs, diagonal stiffeners were set on both sides along the diagonal direction of the middle area of the steel plate, mainly to prevent the out-of-plane buckling of the steel plate. (4) Only the steel plate, diagonal stiffener and periphery stiffener were made of S30408 austenitic stainless steel for stainless SPSWs. Other parts were made of Q235B steel.

3.1.3. SPSW dimensions

The height-thickness ratio λ, stiffness ratio of diagonal stiffener η_s and stiffness ratio of periphery stiffener η_f were key factors affecting the hysteresis behavior of SPSWs. Combined with the construction form of the test specimens, λ, η_s and η_f could be calculated by Eqs. (8), (9) and (12). The geometric dimensions of the test specimen are shown in Fig. 8(b).

$$\lambda = \frac{H_e}{t_w} \tag{8}$$

$$\eta_s = \frac{2E_s I_s}{D\left(H_e \sin\theta + L_e \cos\theta\right)} \tag{9}$$

$$I_s = \frac{t_s b_s^3}{12} + \left(t_s b_s\right)\left(\frac{b_s}{2}\right)^2 = \frac{t_s b_s^3}{3} \tag{10}$$

$$D = \frac{E_s t_w^3}{12\left(1-\nu^2\right)} \tag{11}$$

$$\eta_f = \frac{\left(1-\nu^2\right) t_f b_f^3}{t_w^3 L_e} \geq 1 \tag{12}$$

where, H_e is the effective height and L_e is the effective width of SPSWs, as shown in Fig. 8(b); I_s is the moment of inertia of the stiffener to the middle surface of the steel plate; D is the out-of-plane stiffness of the steel plate; t_w is the thickness of the steel plate, t_s is the thickness of the diagonal stiffener and b_s is the width of the diagonal stiffener, as shown in Fig. 8(c); t_f is the thickness of the periphery stiffener and b_f is the width of the periphery stiffener, as shown in Fig. 8(d); E_s is the material elastic modulus; ν is the material Poisson ratio; θ is the included angle between the diagonal stiffener and the vertical stiffener, as shown in Fig. 8(b); $(H_e \sin\theta + L_e \cos\theta)$ is the width of the steel plate perpendicular to the stiffener.

Subjected to the limitation of the test loading setup, the similarity ratio of the test specimens was designed as 1:3. The effective height H_e of all specimens was taken as 750 mm and the effective width L_e was taken as 600 mm. The aspect ratio was $\alpha = 600/750 = 0.8$. In the test, the effect of the stiffness ratio of the periphery stiffener η_f on the seismic performance of the specimens was not investigated, so $\eta_f = 60$. The codes, dimensions and parameters to be investigated for each specimen are shown in Table 5. To compare the effect of the presence and absence of diagonal stiffeners on the seismic performance of stainless SPSWs, SW-6 was a stainless SPSW without diagonal stiffeners.

Combined with the purpose of the test, the specimens were divided into three groups: (1) The first group consisted of SW-1, SW-2 and SW-3 to investigate the influence of height-thickness ratio λ on the seismic performance of diagonally stiffened stainless SPSWs; (2) The second group consisted of SW-3, SW-4, SW-5 and SW-6 to investigate

Table 5
Codes, dimensions and parameters to be investigated.

SPSW	Dimensions (mm)					Parameters to be Investigated		
	t_w	t_s	b_s	t_f	b_f	λ	η_s	Material
SW-1	2.0	3.0	22	3.0	47	375	30	S30408 austenitic stainless steel
SW-2	2.5	3.0	27	3.0	58	300	30	
SW-3								S30408 austenitic stainless steel
LYSW	3.0	3.0	33	3.0	70	250	30	LY100 low-yield-strength steel
CSW								Q235B steel
SW-4	3.0	3.0	23	3.0	70	250	10	
SW-5	3.0	3.0	18	3.0	70	250	5	S30408 austenitic stainless steel
SW-6	3.0	/	/	3.0	70	250	/	

the influence of stiffness ratio of diagonal stiffeners η_s; (3) The third group consisted of SW-3, LYSW and CSW to investigate the influence of material types.

3.2. Test setup

A four-bar linkage loading setup shown in Fig. 9 was used in the test, which included a horizontal actuator, foundation beam, L-shaped loading beam, four-bar linkage system and lateral bracing. The four-bar linkage system could restrict the in-plane rotation of the L-shaped loading beam without consuming the shear provided by the horizontal actuator and could satisfy the boundary conditions of the test specimens. The lower end of the specimens was fixed, and the upper end slid directionally. Lateral bracing could prevent the L-shaped loading beam from laterally moving out of plane. To prevent the lateral bracing from consuming the shear provided by the horizontal actuator, directional pulleys were used to contact the lateral bracing and the L-shaped loading beam. In the test, SPSWs were 1:3 scale specimens, and the total height of the specimens was 970 mm. The height of the left vertical part of the L-shaped loading beam was 1800 mm. Therefore, to prevent the L-shaped loading beam from contacting the foundation beam, the overall height of the specimens should be more than 1800 mm. To satisfy the distance and ensure the effective connection between the specimens and the loading device, transition beams and struts were added around the specimens as auxiliary loading devices. The upper transition beam was connected with the L-shaped loading beam and the lower transition beam was connected with the foundation beam by M24 high-strength bolts. The upper and lower ends of the specimens were connected with the transition beams by M20 high-strength bolts. To prevent consuming the shear provided by the loading device, the upper and lower ends of the struts were connected with the transition beams by pin shafts.

3.3. Arrangement of displacement gauges

Three displacement gauges D1, D2 and D3 were arranged, as shown in Fig. 10. D3 was arranged at the bottom of the specimen to measure the bottom horizontal displacement. D1 and D2 were arranged on the top of the specimen to measure the top horizontal displacement. The D-value between the average of D1 and D2 with D3 was the horizontal displacement of the specimen.

3.4. Initial geometric imperfection of SPSWs

The thickness of the test SPSWs was thin and the initial geometric imperfection such as out-of-plane buckling and deformation would inevitably occur during manufacturing, which would have a non-negligible influence on the bearing capacity and hysteresis performance of the SPSWs. In addition, the initial geometric imperfection of the specimens needed to be considered in the subsequent finite element analysis.

To measure the out-of-plane initial geometric imperfection of the SPSWs and facilitate the observation of later test phenomena, 75 mm × 60 mm meshes were drawn on the SPSWs, as shown in Fig. 11(a). The longitudinal axis was represented by A~I with a distance of 75 mm. The horizontal axis was represented by 1~9 with a distance of 60 mm. The test specimen after meshing is shown in Fig. 11(b). A thin horizontal line at the same height of the left and right peripheral stiffeners corresponding to each horizontal axis (A~I) was pulled. Then, a vernier caliper was used to measure the distance between the intersection of each horizontal axis and the longitudinal axis and the horizontal line. The extended width of the left and right peripheral stiffeners corresponding to the height of each horizontal axis was also measured. The D-value between the two was the geometric imperfection of the steel plate at each intersection. The out-of-plane initial geometric imperfection is shown in Fig. 12. The maximum value of the D-values was the maximum out-of-plane initial geometric imperfection amplitude, as shown in Table 6.

Table 6
The maximum imperfection amplitudes of test SPSWs.

SPSW	Imperfection amplitude/mm	SPSW	Imperfection amplitude/mm
SW-1	6.27	SW-5	4.29
SW-2	5.27	SW-6	5.96
SW-3	4.48	LYSW	2.87
SW-4	2.95	CSW	3.22

3.5. Loading system

According to JGJT101-2015 Specification for Seismic Test of Buildings [46], a quasi-static test is generally carried out using load and deformation control. However, for the stainless SPSWs, the stress–strain curve of stainless steel had a strong nonlinearity and no obvious yield platform, so it was difficult to determine the yield load and yield displacement.

A monotonic loading analysis of stainless SPSWs was carried out to obtain the load–displacement curve using the finite element software ABAQUS. The results showed that no obvious yield strength existed in the load–displacement curve. Therefore, in the test, displacement loading was used. Referring to the loading systems in Refs. [47–49], cyclic loading was carried out under the control of the displacement angle during the test. According to existing test results, for steel specimens, the performance was stable after loading 2~3 times for each level during cyclic loading. Therefore, cyclic loading was carried out 3 times from the first stage to the third stage and 2 times for the subsequent stages. The specific loading system is shown in Fig. 13. The displacement angle θ of each specimen can be calculated by Eq. (13).

$$\theta = \frac{\Delta}{H_0} \tag{13}$$

where, Δ is the overall horizontal lateral displacement of the specimen; H_0 is the specimen height, which is 950 mm.

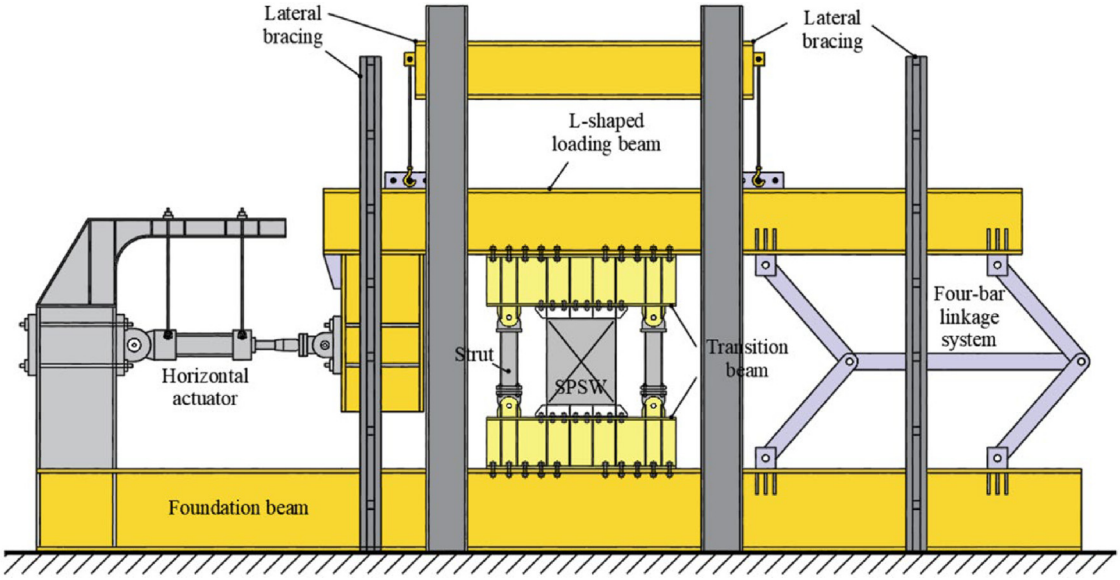

Fig. 9. Test setup.

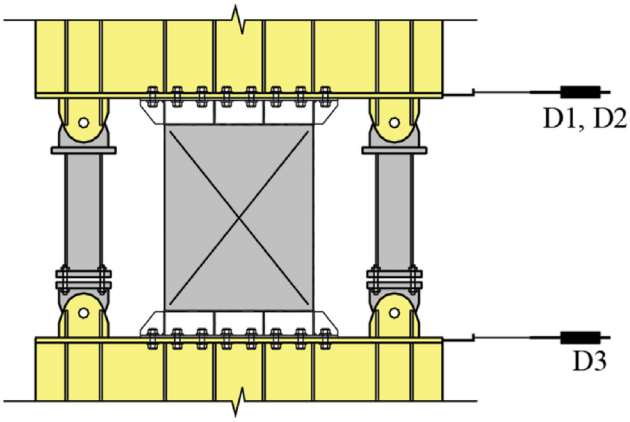

Fig. 10. Displacement gauges.

4. Experimental results and discussion

4.1. Experimental phenomena

The failure phenomena of each test specimen are shown in Fig. 14. The failure modes of the 6 stainless SPSWs are similar, while the failure modes of the low-yield-strength SPSW and Q235 SPSW are significantly different.

At the beginning of loading ($\theta \leq 1/250$), no obvious buckling of the 8 SPSWs occurred. At this time, the SPSWs were in an elastic state, and the hysteresis curves were straight, as shown in Fig. 15.

In the middle stage of loading ($1/250 < \theta \leq 1/50$), (1) for specimens SW-1~SW-5, when θ reached approximately 0.70%, the steel plate had a slight out-of-plane deformation, but no buckling of the diagonal stiffener occurred. As the loading continued, the local buckling of the steel plate became increasingly obvious. When θ reached approximately 1.10%, the buckling of the left and right peripheral stiffeners and the diagonal stiffener began to appear, while the deformation of the diagonal stiffener was smaller. The middle area of the steel plate tended to shrink inward. When θ reached approximately 1.50%, the buckling of the diagonal stiffener became more marked, and the overall deformation of the specimen was transformed from local buckling of the steel plate to global–local buckling. When θ reached approximately 2.00%, an obvious tension field at the diagonal of the steel plate appeared and the deformation of the specimen was transformed to global buckling. At this time, when the horizontal displacement was near the zero point, the buckling wave of the steel plate rapidly switched between the positive and negative directions. (2) For specimen SW-6, because there was no diagonal stiffener, the buckling of the steel plate occurred earlier. When θ reached approximately 1.10%, an obvious tension field was generated. When θ reached approximately 2.00%, a crease was generated at the intersection of the positive and negative tension fields of the steel plate. (3) For specimen LYSW, when θ reached approximately 1.00%, the buckling of the steel plate was significant. When the positive displacement amplitude was reached at this stage, the peripheral stiffener at the lower left corner was torn. When the negative displacement amplitude was reached, the peripheral stiffener at the upper left corner was torn, as shown in Fig. 14(h). At this time, it could be seen from the skeleton curve that the bearing capacity reached the maximum, as shown in Fig. 16(c). When θ reached approximately 1.50%, buckling occurred in the middle of the diagonal stiffener. The bearing capacity of the specimen decreased, but no obvious pinch appeared. (4) For specimen CSW, slight out-of-plane buckling of the steel plate occurred at the beginning, but the deformation was not significant. When θ reached approximately 0.90%, the buckling of the steel plate became more obvious, and slight buckling of the peripheral stiffener occurred. At this time, the bearing capacity of the specimen reached the maximum, as shown in Fig. 16(c). When θ reached approximately 1.50%, the buckling of the steel plate increased. When the positive displacement amplitude was reached at this stage, the peripheral stiffeners at the upper right corner and the lower left corner were torn. When the negative displacement amplitude was reached, the peripheral stiffeners at the upper left corner and the lower right corner were torn, as shown in Fig. 14(j). The bearing capacity of the specimen decreased, but no obvious pinch appeared.

At the later stage of loading ($\theta > 1/50$), (1) for specimens SW-1~SW-6, θ of the specimen exceeded the value of 1/50 required by JGJT101-2015 Specification for Seismic Test of Buildings [46]. For stainless SPSWs, when θ reached 2.45%, significant buckling of the steel plate and the diagonal stiffener (specimen SW-6 excluded) occurred, and an out-of-plane rotation of the peripheral stiffener occurred. When θ reached approximately 3.00%, the shrinkage in the middle area of the steel plate was aggravated, and the tension field was more significant. (2) For specimen LYSW, when θ reached approximately 2.15%, a serious tearing occurred at the upper right and lower right corners, as

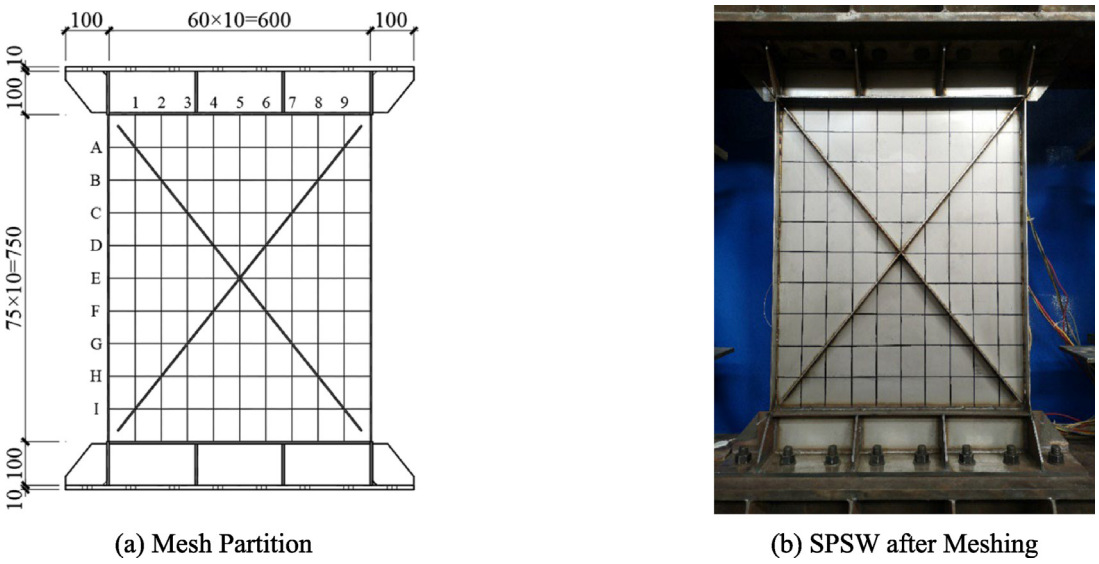

Fig. 11. Mesh partition of initial geometric imperfection measurement.

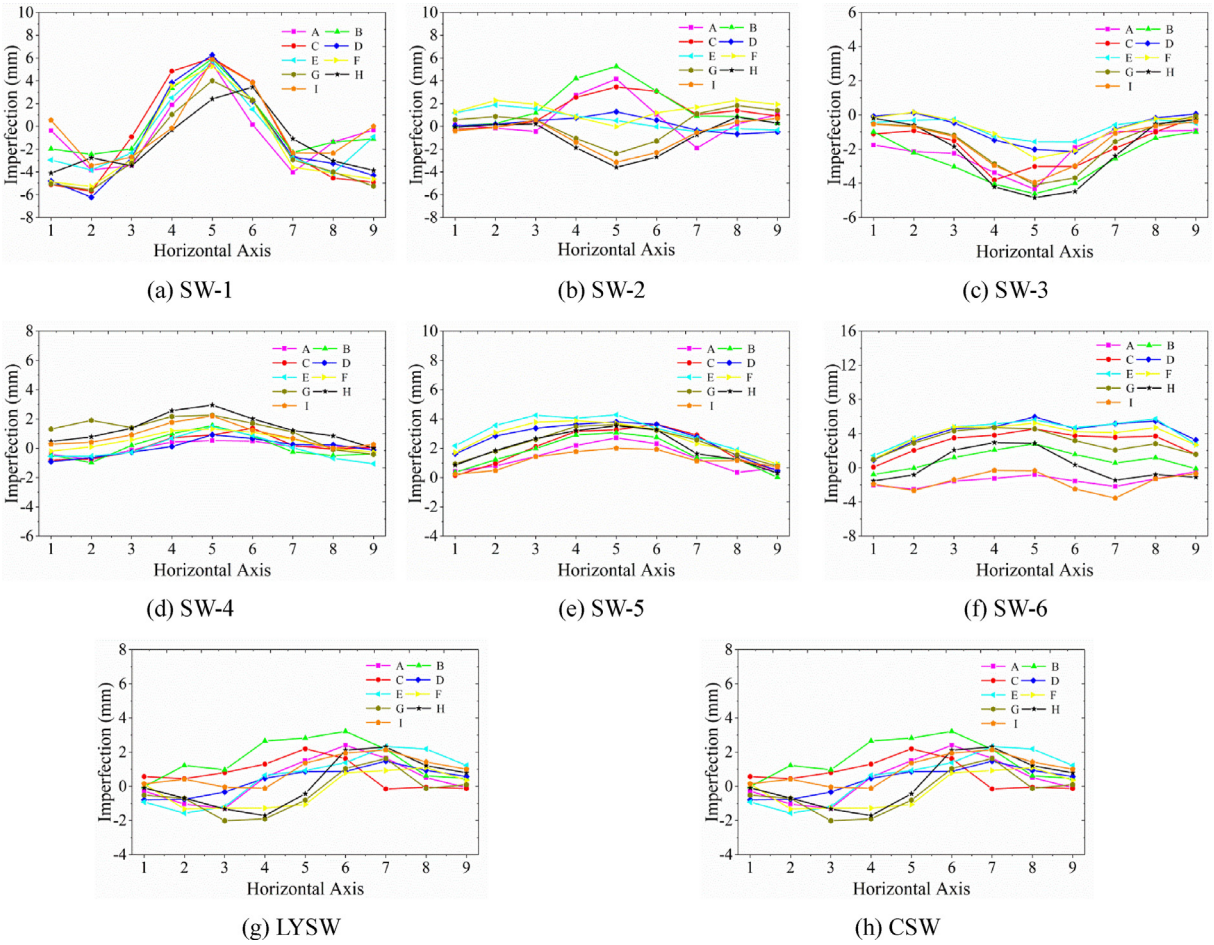

Fig. 12. Out-of-plane initial geometric imperfection.

shown in Fig. 14(h). When θ reached approximately 2.70%, the overall deformation of the specimen was very serious and the bearing capacity dropped below 85% of the maximum, so the test was stopped. (3) For specimen CSW, when θ reached approximately 2.20%, the corner tearing became more serious. The bearing capacity of the specimen decreased significantly, which was lower than 85% of the maximum. The test was stopped.

Overall, during the test, (1) for stainless SPSWs, good ductility and steel plate tension field were observed, and no corner tearing occurred. No significant decrease in the bearing capacity occurred and

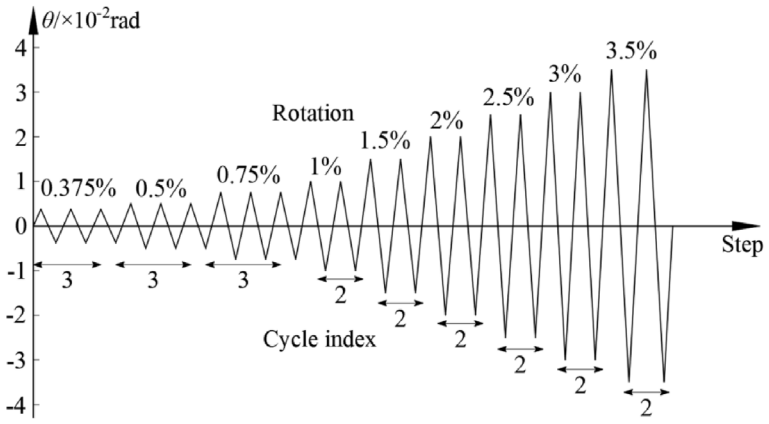

Fig. 13. Loading system of test SPSWs.

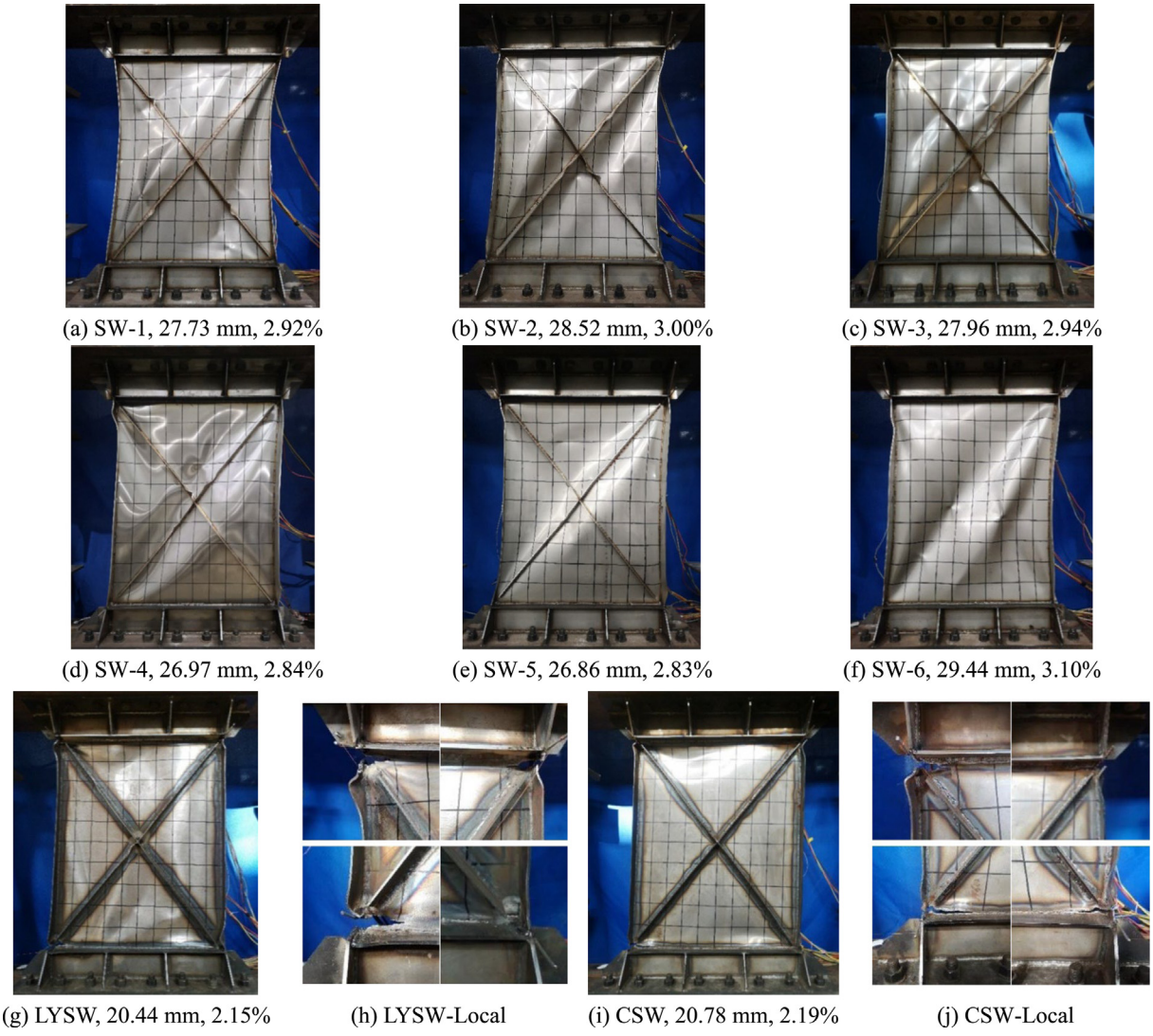

Fig. 14. Failure phenomena (specimen, displacement, θ).

the existence of diagonal stiffener could delay the buckling of the steel plate. (2) For the low-yield-strength SPSW and Q235 SPSW, obvious corner tearing and poor ductility were observed. In the later stage of loading, the bearing capacity decreased significantly.

4.2. Hysteresis curve

The hysteresis curve is the most basic index used to evaluate the seismic performance of members. The test results of the hysteresis

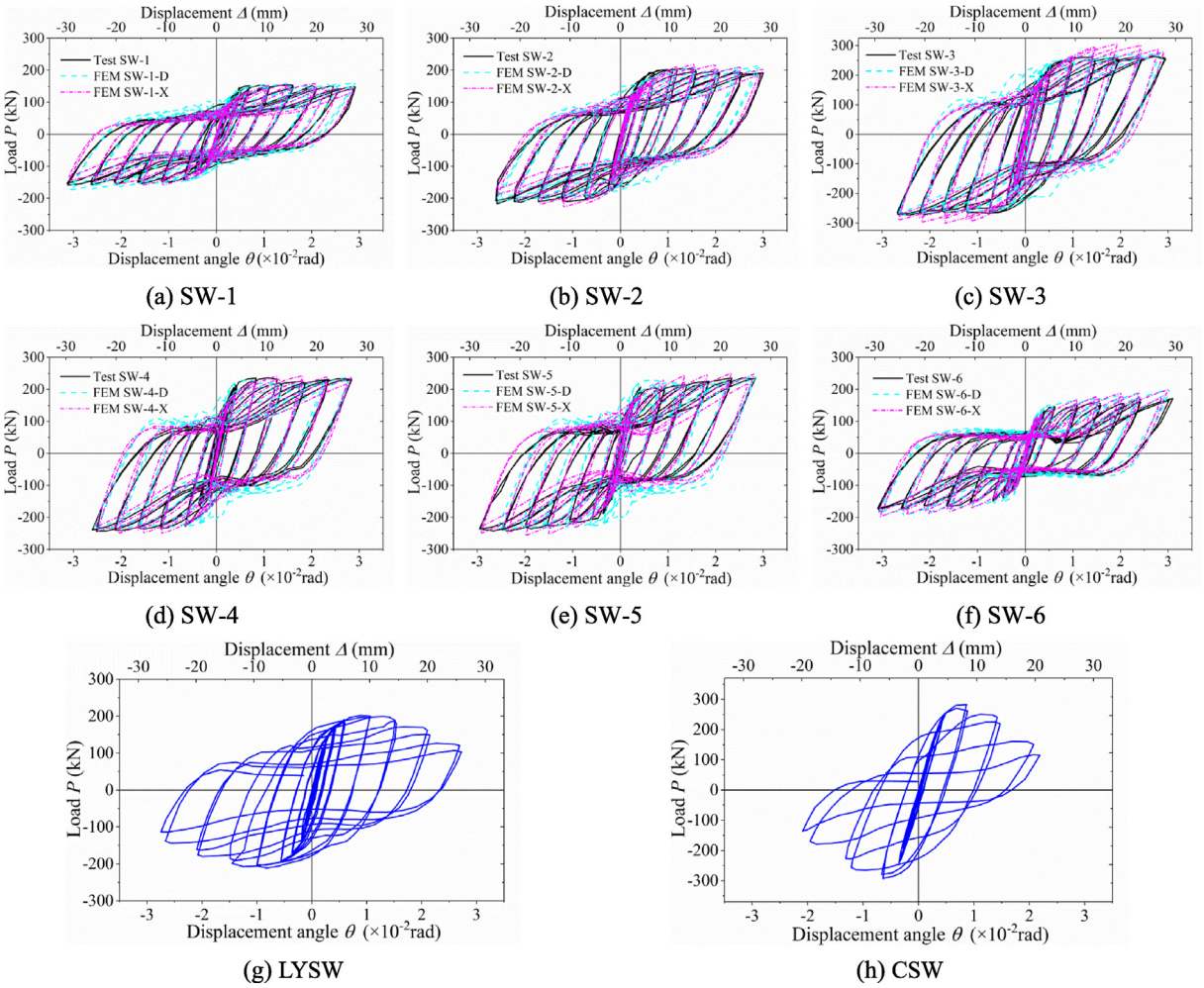

Fig. 15. Hysteresis curves.

curves of the 8 SPSWs are shown in Fig. 15. To facilitate comparison, the coordinate axes of the hysteretic curves are as consistent as possible.

According to the comparison of specimens SW-1, SW-2 and SW-3, it can be seen that (1) in the middle and later stages of loading, different levels of pinch appear. (2) For specimen SW-1, the hysteresis curve area is the smallest, the absorbed energy is the smallest and the pinch is the most serious. For specimen SW-3, the hysteresis curve area is the largest, the energy absorbed is the largest and the pinch is the lightest. The results show that the smaller the height-thickness ratio λ is, the stronger the energy absorption and dissipation capacity are. (3) An obvious pinch of the hysteresis curves of specimens SW-1~SW-3, respectively appear from θ at 1.0%, 1.5% and 2.0%, indicating that the pinch is gradually delayed with λ decreasing.

According to the comparison of specimens SW-3~SW-6, it can be seen that (1) for specimen SW-6, the pinch of the hysteresis curve is more significant than those of specimens SW-3~SW-5. A shuttle shape with sawtooth of the hysteresis curve is presented. When the displacement is near the zero point, zero stiffness or even negative stiffness appears. The reasons are as follows: under the horizontal cyclic load, the buckling of specimen SW-6 without a stiffener occurs more easily, and a tension field is formed. Additionally, a great deformation of the steel plate is presented. When the load is reversed, the tension field is relaxed or even compressed, and a great mutation deformation of the steel plate occurs, resulting in zero stiffness or even negative stiffness of the steel plate. (2) Compared with specimen SW-6, specimens SW-3~SW-5 can effectively prevent the out-of-plane buckling of the steel plate to improve the energy dissipation. (3) For specimens SW-3~SW-5, the pinch of the hysteresis curves becomes increasingly serious, and the energy dissipation worsens as the diagonal stiffener stiffness ratio η_s decreases.

According to the comparison of specimens SW-3, LYSW and CSW, it can be seen that (1) compared with specimens SW-3 and CSW, the hysteresis loop of specimen LYSW forms the earliest and the hysteresis curve is the fullest, indicating that an earliest yield and a greatest energy dissipation of the low-yield-strength steel appear. (2) Compared with specimen SW-3, the peak points of the hysteresis curves of specimens LYSW and CSW decrease significantly subjected to the serious tearing of steel plate in the later stage, which indicates that the ductility of specimen SW-3 is the best. (3) For specimens LYSW and CSW, in the later stage, a great difference of the hysteresis curves between the two cycles of loading at the same level appears, which indicates that a large plastic damage is accumulated.

4.3. Skeleton curve

The skeleton curve mainly reflects the yield bearing capacity, ultimate bearing capacity and relative changes between force and displacement during loading. The test results of the skeleton curves of the three groups of specimens are shown in Fig. 16.

Fig. 16(a) shows that the initial slope of the skeleton curves, the initial stiffness and the bearing capacity of the specimens increase with decreasing height-thickness ratio λ.

Fig. 16(b) shows that (1) the initial slope of the skeleton curves of specimens SW-3~SW-5 is nearly the same, but the later load decreases as the stiffness ratio of diagonal stiffener η_s decreases. The initial slope

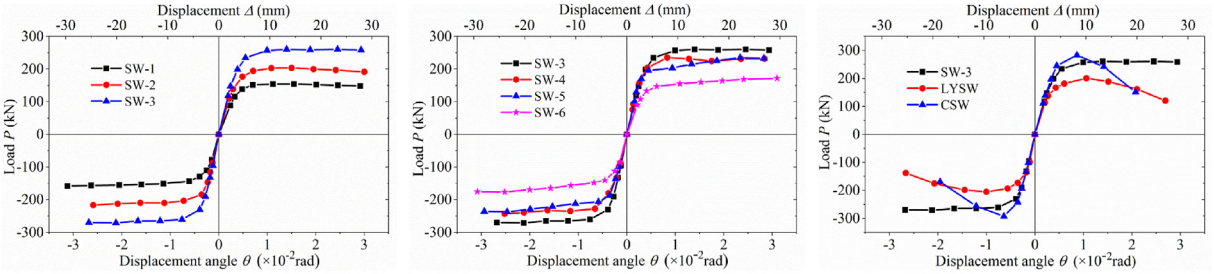

(a) First Group of Specimens (b) Second Group of Specimens (c) Third Group of Specimens

Fig. 16. Skeleton curves of three groups of specimens.

of the skeleton curve of specimen SW-6 is the lowest, indicating that the diagonal stiffener can prevent the out-of-plane buckling of the specimen at the initial stage of loading to improve the initial stiffness of the specimen. However, when the stiffness ratio of the diagonal stiffener increases to a certain extent, the influence on the initial stiffness is relatively smaller. (2) The skeleton curves increase slightly in the later stage as the stiffness ratio of diagonal stiffener η_s increases, indicating that the stiffener plays a positive role in the formation of the tension field and improves the bearing capacity of the specimen.

Fig. 16(c) shows that (1) the initial slope and peak point of the skeleton curve of specimen CSW are slightly higher than those of specimens SW-3 and LYSW. (2) The skeleton curve of specimen SW-3 increases slightly in the later stage and the skeleton curves of specimens LYSW and CSW decrease significantly in the later stage, especially for specimen CSW, which indicates that the ductility of specimens LYSW and CSW is poor. The main reason for this phenomenon is that the ductility of stainless steel is better than that of low-yield-strength steel and Q235 steel.

4.4. Ductility coefficient

Ductility is an important index to reflect the plastic deformation of structures or members. To quantitatively compare the ductility of each specimen, the concept of the ductility coefficient is introduced. The ductility coefficient refers to the ratio of the ultimate displacement Δ_u and yield displacement Δ_y, which can be calculated by Eq. (14).

$$\mu = \frac{\Delta_u}{\Delta_y} \tag{14}$$

where, Δ_u is the deformation corresponding to 85% of the maximum load V_{max}. For the specimen whose bearing capacity is not reduced to 0.85 V_{max}, the maximum displacement is taken for calculation; Δ_y is the yield displacement, which can be determined by the geometric graphic method, as shown in Fig. 17. Where, OA is the tangent of the skeleton curve; D is the peak point; AD is the horizontal line; AB is the vertical line; C is the intersection of OB and AD; CE is the vertical line; E is the yield point.

The characteristic coefficients of each SPSW are shown in Table 7. Table 7 shows that the ductility coefficients of specimens SW-1~SW-6 are significantly higher than those of specimens LYSW and CSW. For specimens SW-1~SW-3, the ductility decreases slightly with decreasing height-thickness ratio, while the influence of the stiffness of the diagonal stiffener on the ductility coefficient is small.

4.5. Energy dissipation

Energy dissipation refers to the ability of a structure or member to absorb energy subjected to plastic deformation under an earthquake. Since Jacobson put forward the concept of the equivalent viscous damping ratio ζ in 1930, ζ has been widely used in earthquake engineering to

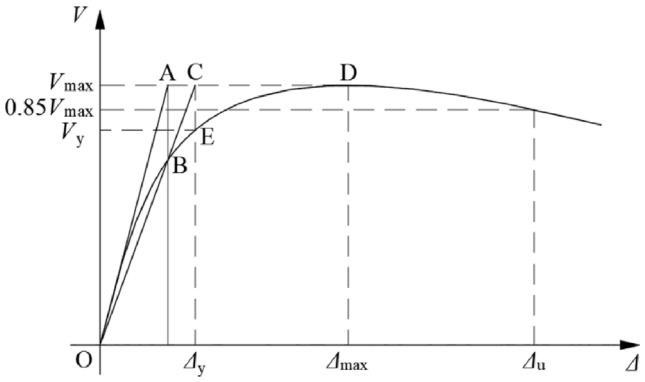

Fig. 17. Yield displacement determined by geometric graphic method.

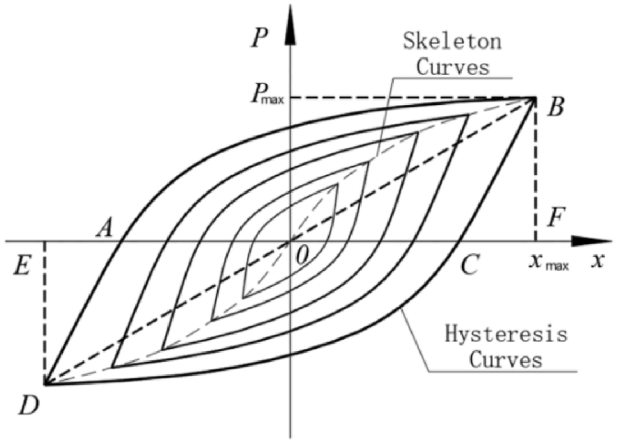

Fig. 18. Typical hysteresis curves.

express the energy dissipation of a structure or member. ζ is calculated by Eq. (15).

$$\zeta = \frac{1}{2\pi} \cdot \frac{S_{ABC} + S_{CDA}}{S_{OBF} + S_{ODE}} \tag{15}$$

where, S_{ABC} and S_{CDA} are the area enclosed by the hysteresis curve, as shown in Fig. 18; $S_{\Delta OBF}$ and $S_{\Delta ODE}$ are the area of triangle OBF and ODE, as shown in Fig. 18.

The equivalent viscous damping ratio ζ - displacement angle θ curves of the three groups of specimens are shown in Fig. 19. It can be seen that (1) the development trend of the ζ - θ curves is the same, and the curves increase first and then decrease. (2) A gradual transformation from an elastic stage to an elastic–plastic stage is presented, and a final energy dissipation stage subjected to a post buckling tension field is formed.

Table 7
Ductility coefficients of each SPSW.

SPSW	Loading direction	Yield load V_y/kN	Peak load V_{max}/kN	Yield displacement Δ_y/mm	Ultimate displacement Δ_u/mm	Ductility coefficient μ
SW-1	Positive	140.73	153.89	4.90	27.73	5.66
	Negative	−128.65	−156.33	−3.67	−29.63	6.81
SW-2	Positive	188.75	203.20	6.13	28.52	4.66
	Negative	−186.10	−212.14	−3.64	−24.59	5.43
SW-3	Positive	240.26	260.23	6.36	27.90	4.39
	Negative	−233.65	−270.88	−4.11	−25.45	4.90
SW-4	Positive	211.93	234.80	5.06	26.97	5.33
	Negative	−199.41	−239.44	−4.65	−23.94	4.33
SW-5	Positive	197.73	234.59	5.84	26.86	4.60
	Negative	−198.37	−237.34	−4.62	−27.92	5.07
SW-6	Positive	146.05	171.24	5.80	29.44	5.08
	Negative	−136.97	−176.54	−4.03	−29.27	5.93
LYSW	Positive	185.12	200.25	6.62	14.39	2.75
	Negative	−164.65	−205.33	−4.00	−14.71	3.68
CSW	Positive	251.80	282.60	5.00	13.50	2.71
	Negative	−261.17	−292.80	−4.38	−11.52	2.63

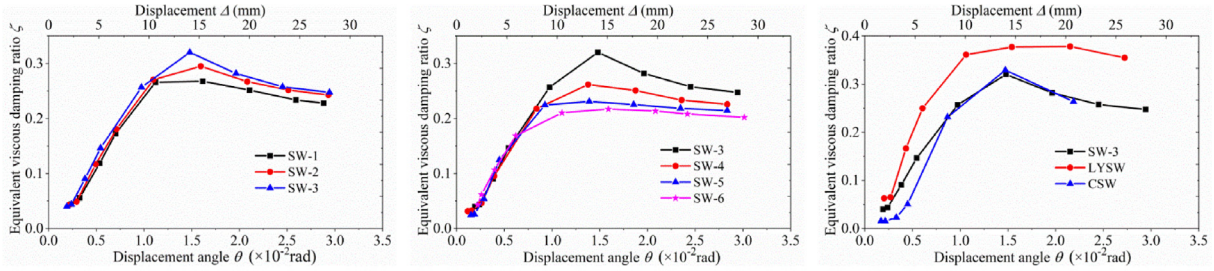

(a) First Group of Specimens (b) Second Group of Specimens (c) Third Group of Specimens

Fig. 19. Equivalent viscous damping ratio ζ - Displacement angle θ curves.

Fig. 19(a) shows that (1) when $\theta \leq 0.25\%$, the ζ of specimens SW-1~SW-3 is small, and ζ increases slowly with increasing θ. At this time, the specimens are in an elastic state, the hysteresis curves of the specimens are straight, and little external energy is absorbed, so ζ is small and the growth rate is also small. (2) When $0.25\% \leq \theta \leq 1.50\%$, ζ increases rapidly with increasing θ, indicating that a rapid transformation from an elastic state to an elastic–plastic state of the specimens occurs. (3) When $\theta \geq 1.50\%$, ζ decreases slowly with increasing θ. At this time, the overall buckling of the specimens is serious, and the energy dissipation is reduced, but the curve decreases slowly when subjected to the formation of a tension field. (4) ζ of specimens SW-1~SW-3 increases in turn, indicating that the energy dissipation improves as λ decreases.

Fig. 19(b) shows that (1) when $\theta \leq 0.25\%$, the ζ - θ curves are similar to those of the first group. (2) When $0.25\% \leq \theta \leq 0.75\%$, the growth of the ζ - θ curves is the same, indicating that the influence of the stiffness ratio of the diagonal stiffener η_s on the energy dissipation is small when $\lambda = 300$. (3) When $0.75\% \leq \theta \leq 1.50\%$, the growth rate of ζ of specimens SW-3~SW-6 decreases as η_s decreases. At this stage, the diagonal stiffeners become increasingly significant, which can effectively prevent the out-of-plane buckling of the steel plate to improve the energy dissipation of the specimens. (4) When $\theta \geq 1.50\%$, ζ decreases slowly with increasing θ. For specimen SW-6, the ζ - θ curve is nearly horizontal in the later stage. The ζ - θ curves of specimens SW-3~SW-5 at the later stage gradually move toward that of specimen SW-6, indicating that the buckling of the diagonal stiffener is more serious and that the diagonal stiffener has stopped working at the later stage of loading. The energy dissipation is mainly borne by the tension field.

Fig. 19(c) shows that (1) when $\theta \leq 0.25\%$, the ζ - θ curves are similar to those of the first group. (2) When $0.25\% \leq \theta \leq 1.0\%$, ζ increases rapidly with increasing θ, indicating that a rapid transformation from an elastic state to an elastic–plastic state occurs. ζ of specimen LYSW is the largest, and ζ of specimen CSW is the smallest, indicating that the lower the yield strength of the steel, the earlier it enters an elastic–plastic energy dissipation stage. A strong nonlinearity of stainless steel is shown, which leads to an earlier elastic–plastic stage of specimen SW-3 than specimen CSW. (3) When $\theta \geq 1.0\%$, the difference between the curves of specimen SW-3 and specimen CSW is small. At this stage, the advantage of the energy dissipation of stainless steel is not obvious. (4) The ζ - θ curve of specimen LYSW is higher than that of specimen SW-3 and specimen CSW, indicating incomparable advantages of the energy dissipation of low-yield-strength steel.

5. Finite element analysis

5.1. Finite element model

A refined finite element model of the stainless SPSWs was established using the software ABAQUS. The geometric model of the specimen was mainly composed of 6 parts: steel plate, diagonal stiffener, peripheral stiffener, end stiffener, normal stiffener and connection plate, which were simulated by S4R shell element, as shown in Fig. 20(a). The automatic meshing technology was adopted, and the mesh size was finally controlled below 10 mm after a mesh sensitivity analysis, as shown in Fig. 20(b).

The boundary conditions and loading system were consistent with the test. The bolt holes of the upper and lower connection plates of the SPSW were coupled to two reference points, respectively. The displacement constraints in Y and Z directions and rotation constraints in X, Y and Z directions were applied to the upper reference point. While the displacement constraints and rotation constraints in all directions were applied to the lower reference point. The upper end of the SPSW was a directional support and the lower end was a fixed support. The

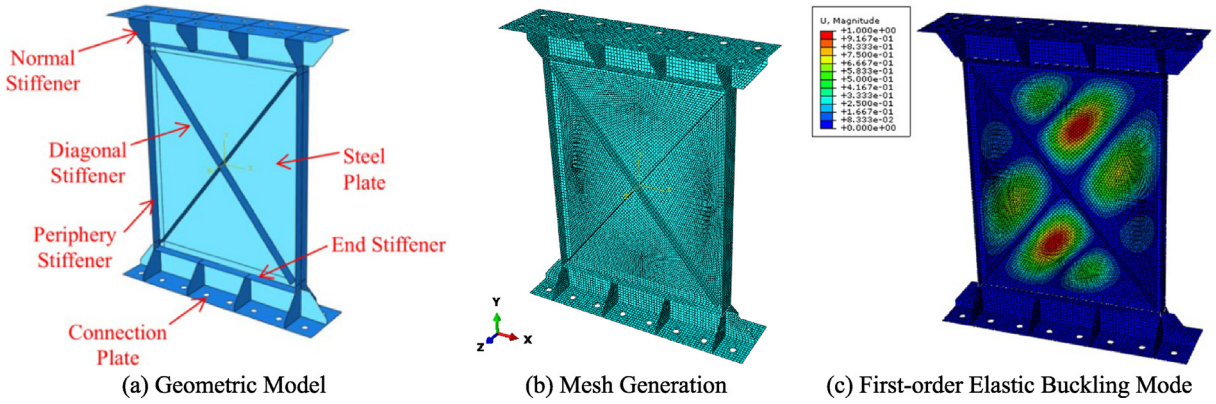

Fig. 20. Geometric model, mesh generation and first-order elastic buckling mode.

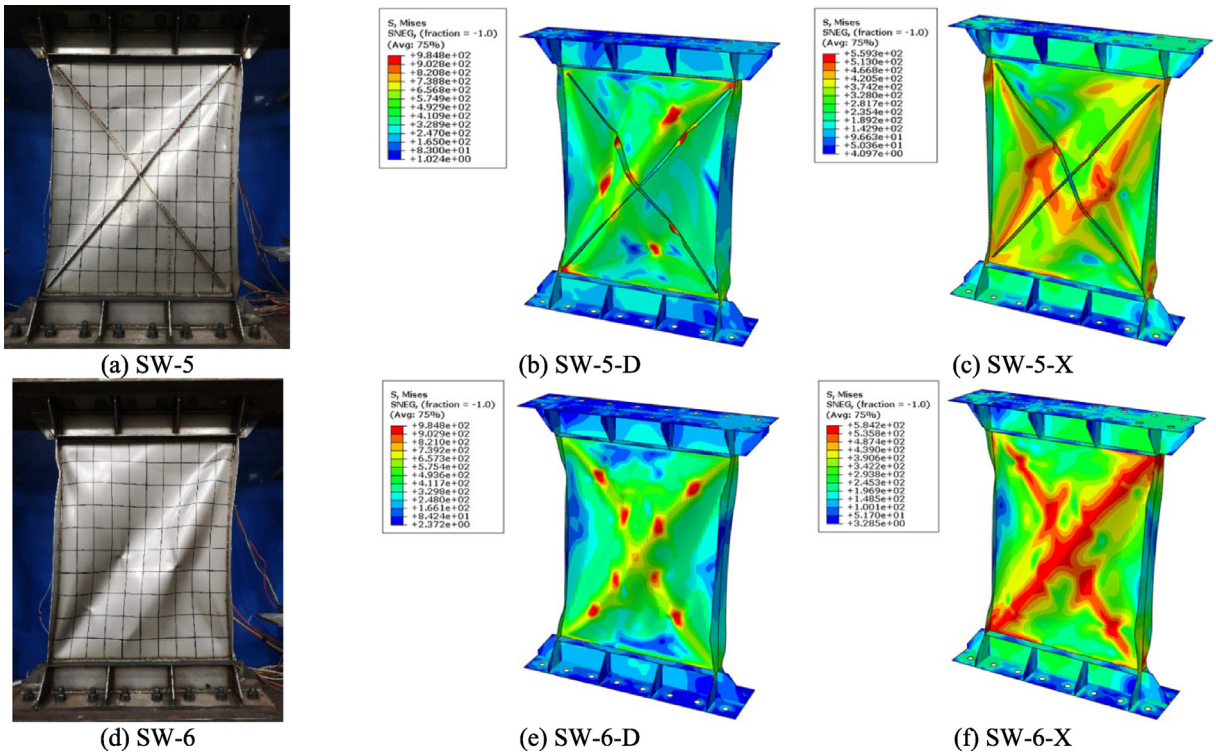

Fig. 21. Comparison of the failure phenomena.

initial geometric imperfection measured in Table 6 was introduced using the distribution of the first-order elastic buckling mode, as shown in Fig. 20(c).

The seismic behavior of each specimen with material constitutive models under monotonic loading and cyclic loading was obtained respectively. The constitutive model of stainless steel under monotonic loading and cyclic loading adopted the average values of the test, which were illustrated in Section 2.

5.2. Finite element verification

Since the failure modes of stainless SPSWs are similar, only the comparison between the finite element results and test results of the failure phenomena of specimens SW-5 and SW-6 is shown in Fig. 21, where D stands for the finite element model with material constitutive model under monotonic loading and X stands for the finite element model with material constitutive model under cyclic loading. Due to the thin stainless steel plates, asymmetric deformation was inevitable during manufacturing and transportation. However, these effects cannot be considered in the initial geometric imperfection introduced by the first-order elastic buckling mode. For SW-6, there is no diagonal stiffener which leads to a more obvious difference. Overall, it can be seen from Fig. 21 that the tension field formed by the stainless SPSW model using the material constitutive model under cyclic loading is more accurate and the stress is more concentrated in the tension field.

The comparison between the finite element results and test results of the hysteresis curves is shown in Fig. 15, where D and X stands for the same meaning as above. It can be seen from Fig. 15 that: (1) the finite element results of the two models are in good agreement with the test results. A pinch occurs and a zero stiffness or even negative stiffness near the zero point appears. The finite element results with the material constitutive model under monotonic loading are fuller than the test results, and the finite element results of the load near the zero point are higher than the test results. Compared with the material constitutive model under monotonic loading, the hysteresis curves of the material constitutive model under cyclic loading is closer to the test results. Especially near the zero point, an obvious difference between the finite

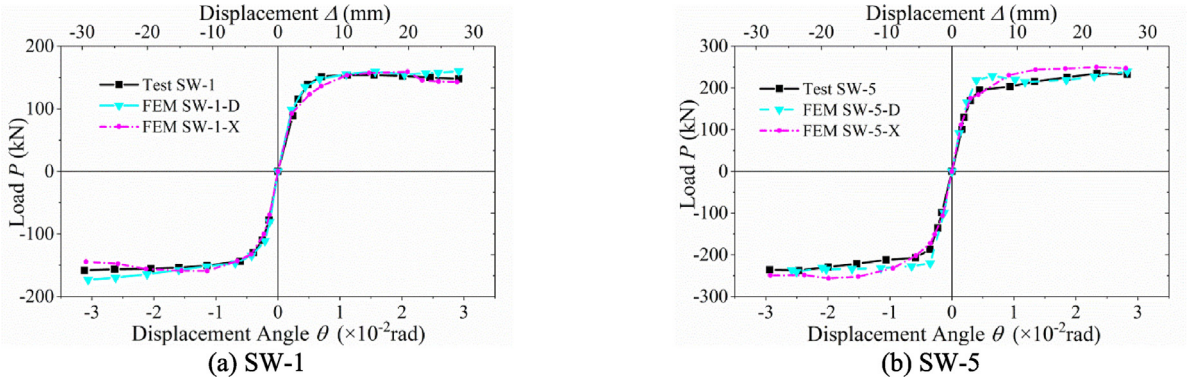

Fig. 22. Skeleton curves.

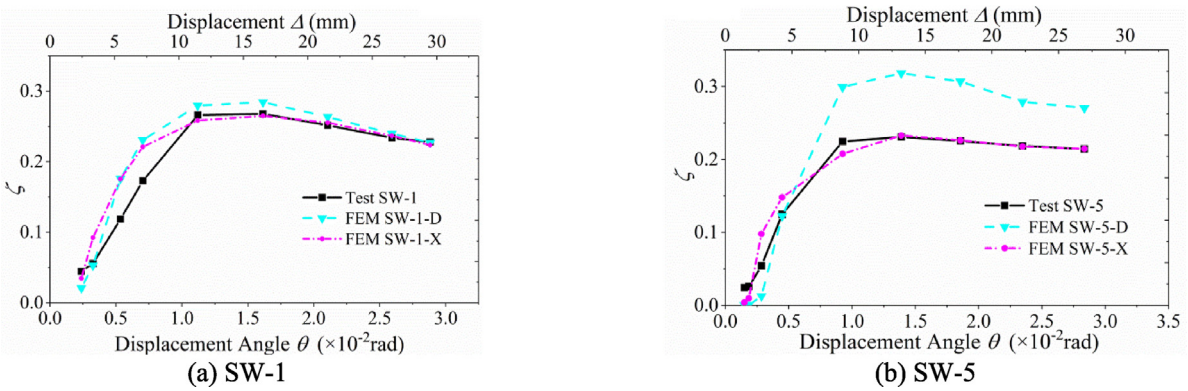

Fig. 23. Equivalent viscous damping ratio ζ - Displacement angle θ curves.

Table 8
Peak load and initial stiffness of stainless SPSWs.

SPSW	Peak load (kN)			Deviation (%)		Initial stiffness (kN/mm)			Deviation (%)	
	Test	FEM-D	FEM-X	DP_{FEM-D}	DP_{FEM-X}	Test	FEM-D	FEM-X	DS_{FEM-D}	DS_{FEM-X}
SW-1	156.3	173.2	159.2	10.81	1.86	46.0	55.1	49.2	13.86	1.70
SW-2	212.1	213.6	226.6	0.71	6.84	60.5	65.3	63.3	3.82	0.69
SW-3	270.9	275.8	300.7	1.81	11.00	71.8	83.9	81.7	13.23	10.21
SW-4	239.4	236.5	250.6	−1.21	4.68	69.6	76.8	75.0	11.13	8.51
SW-5	237.3	241.0	256.4	1.56	8.05	64.9	68.7	68.8	5.91	6.06
SW-6	176.5	199.2	197.6	12.86	11.95	59.5	64.2	57.2	17.60	4.62

Note: 1. FEM-D and FEM-X are the finite element results determined with the material constitutive model under monotonic and cyclic loading, respectively;
2. DP_{FEM-D} = (FEM-D − Test)/Test, DP_{FEM-X} = (FEM-X − Test)/Test, for peak load; DS_{FEM-D} = (FEM-D − Test)/Test, DS_{FEM-X} = (FEM-X − Test)/Test, for initial stiffness.

element results of the material constitutive model under monotonic loading and the test results is presented.

The comparison between the finite element results and test results of the skeleton curves and equivalent viscous damping ratio ζ - displacement angle θ curves is shown in Figs. 22 and 23, where D and X stands for the same meaning as above. Limited to space, only the results of SW-1 and SW-5 were given. It can be seen from Figs. 22 and 23 that: (1) the skeleton curves of the test and two finite element models are very close, especially in the initial loading stage. For SW-5, in the later loading stage, the load of two finite element models is slightly higher than that of the test; (2) for ζ - θ curves, the results of the model under cyclic loading are closer to the test. The results of the model under monotonic loading are higher than that of the test, especially for SW-5.

The comparison of the peak load and initial stiffness between the finite element results and test results is shown in Table 8. It can be seen from Table 8 that: (1) for peak load, both the model under monotonic loading and the model under cyclic loading are in good agreement with the test, and most of the deviations are within 10%; (2) for initial stiffness, the results of the model under cyclic loading are in better agreement with the test.

Overall, the finite element model established herein can accurately simulate the seismic behavior of stainless SPSWs. Compared with the material constitutive model under monotonic loading, the finite element results of the material constitutive model under cyclic loading are closer to the test results. Therefore, in the following research, it is recommended to use the stainless SPSW model established by the material constitutive model under cyclic loading for parametric analysis.

6. Parametric analysis of the hysteretic performance

Based on the verified finite element model, a parametric analysis of the hysteretic performance of diagonally stiffened stainless SPSWs under low cyclic loading was conducted, mainly considering the influence of aspect ratio α, height-thickness λ, stiffness ratio of periphery stiffener η_f and stiffness ratio of diagonal stiffener η_s on the hysteretic performance. The energy dissipation mechanism and characteristics were revealed which provided an important reference for the seismic design of stainless SPSWs.

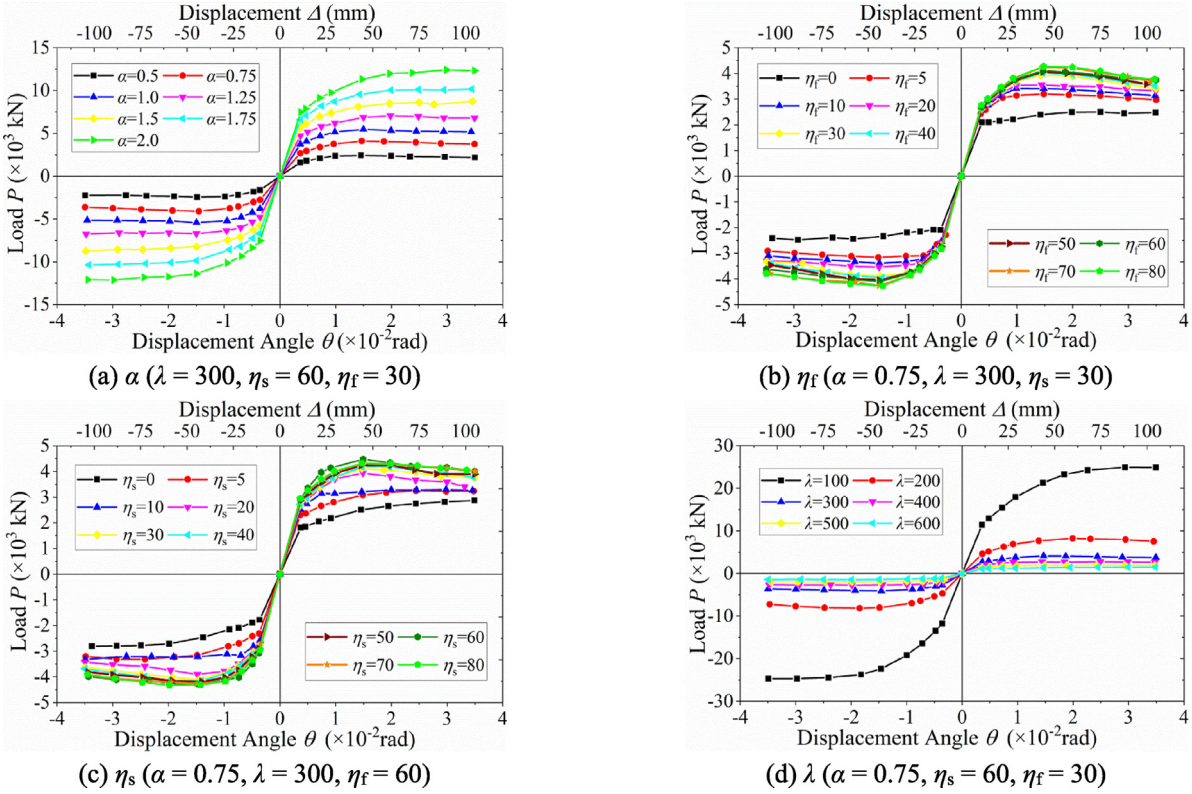

Fig. 24. Skeleton curves of single parameter analysis.

6.1. Single parameter analysis

The skeleton curves of stainless SPSWs with different α, η_f, η_s and λ are shown in Fig. 24. It can be seen from Fig. 24 that: (1) the effective cross sectional area increases with α increasing, leading to an increase of the bearing capacity of stainless SPSWs. When $\alpha < 1.0$, a slight decrease appears. When $\alpha \geq 1.0$, no obvious decrease appears. The larger the α is, the stronger the nonlinearity of the skeleton curves is; (2) when η_f or $\eta_s = 0$, because the side of the SPSW is not restrained, it is easy to have an out of plane buckling under a low load, resulting in a low initial stiffness and yield load. When η_f or $\eta_s < 30$, its effect on the skeleton curves is significant. The bearing capacity of stainless SPSWs decreases with η_f decreasing. When η_f or $\eta_s \geq 30$, its effect on the skeleton curves is small; (3) the effective cross sectional area is determined by λ, so the influence of λ on the skeleton curves is significant. The effective cross sectional area increases with λ decreasing, leading to an increase of the bearing capacity. The smaller the λ is, the stronger the nonlinearity of the skeleton curves is. No obvious decrease of the skeleton curves corresponding to different λ occurs, indicating that stainless SPSWs have a good ductility.

The ζ - θ curves of stainless SPSWs with different α, η_f, η_s and λ are shown in Fig. 25. It can be seen from Fig. 25 that: (1) for different α, when $\theta < 2.0\%$, ζ increases with θ increasing, indicating that the energy dissipation increases. When $\theta \geq 2.0\%$, subjected to the pinch of the hysteresis curves, ζ decreases with θ increasing, indicating that the energy dissipation decreases; (2) for different η_f and η_s, when η_f or $\eta_s < 30$, the ζ - θ curves decrease in the later stage. When η_f or η_s becomes smaller, the decrease occurs earlier. When η_f or $\eta_s \geq 30$, the effect is not significant; (3) for different λ, when $\theta < 0.75\%$, the ζ - θ curves are basically consistent, indicating that no out of plane buckling occurs. when $\theta \geq 0.75\%$, the energy dissipation becomes stronger with λ decreasing. When $\lambda < 300$, no obvious decrease of the ζ - θ curves occurs. When $\lambda \geq 300$, a decrease occurs in the late stage of the ζ - θ curves. When λ becomes larger, the decrease occurs earlier.

6.2. Multi-parameter analysis

The influences of single parameter α, λ, η_f and η_s on the hysteretic performance of stainless SPSWs were analyzed in Section 6.1. The results show that α and λ are important factors affecting the hysteretic performance. When η_f or $\eta_s \geq 30$, the effect is small. Therefore, in the multi-parameter analysis, η_s was taken as 30 for safety. η_f was taken as 60 to prevent the periphery stiffener from buckling earlier than the diagonal stiffener. α was taken as 0.5, 0.75, 1.0, 1.25, 1.5, 1.75 and 2.0 and λ was take as 100, 200, 300, 400, 500 and 600. The height H_e of SPSWs was uniformly taken as 3000 mm, with a total of 42 models.

The skeleton curves are shown in Fig. 26. It can be seen from Fig. 26 that: (1) an obvious nonlinearity of the skeleton curves of SPSWs appears and no significant decrease occurs in the later stage of loading, indicating that stainless SPSWs have a good ductility; (2) when λ is constant, the effective cross sectional area of SPSWs increases with α increasing, resulting in an increase of the bearing capacity of SPSWs. The increase of load at each characteristic point is approximately the same, indicating that the bearing capacity is approximately linear with α; (3) λ is the key factor affecting the skeleton curves of stainless SPSWs. The effective cross sectional area decreases with λ increasing, resulting in a decrease of the peak load.

The energy dissipation curves are shown in Fig. 27. It can be seen from Fig. 27 that: (1) when $\lambda = 100$, ζ corresponding to different α increases with θ increasing. When $\theta < 0.5\%$, ζ increases fast. When $\theta \geq 0.5\%$, ζ increases slowly; (2) When $\lambda \geq 200$, ζ corresponding to different α increases fast at the beginning and then decreases slowly with θ increasing. When $\theta < 0.5\%$, ζ increases faster and the ζ - θ curves are basically consistent. When $\theta \geq 0.5\%$, the ζ - θ curves corresponding to different α decrease. Nevertheless, no obvious law appears with α increasing; (3) the influence of λ on ζ is greater than that of α, indicating that λ is the key factor affecting the energy dissipation of stainless SPSWs.

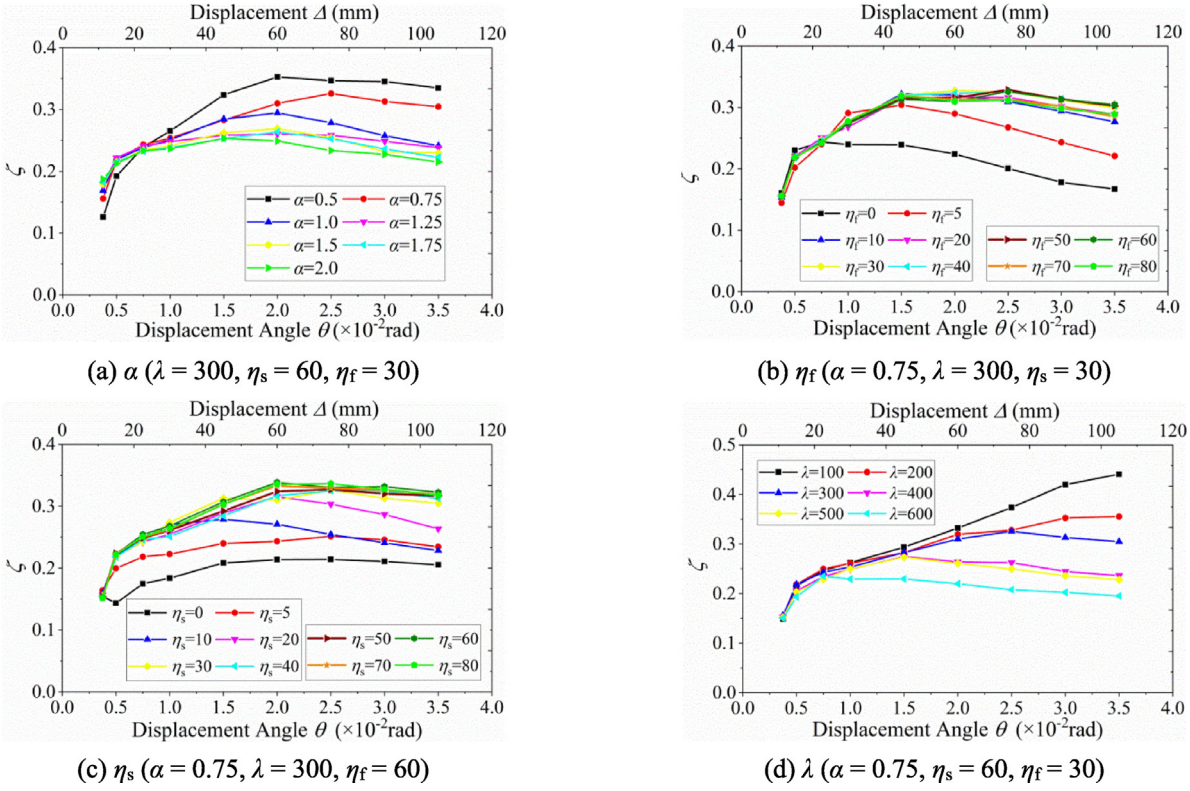

Fig. 25. ζ - θ curves of single parameter analysis.

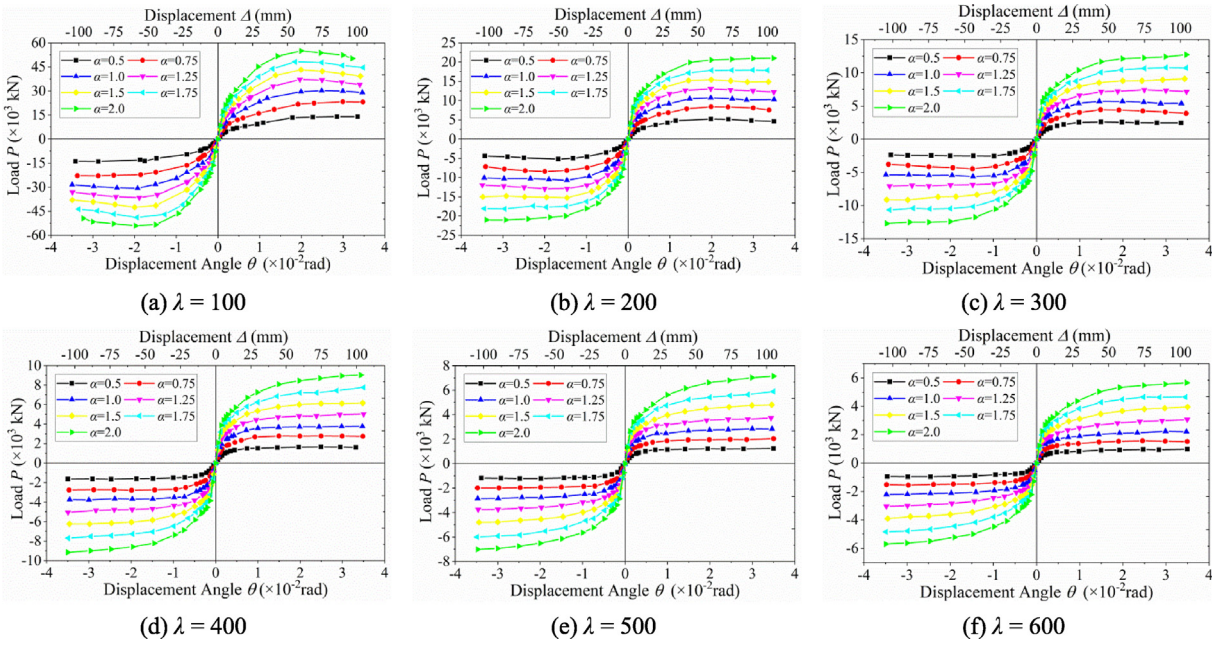

Fig. 26. Skeleton curves of multi-parameter analysis.

7. Limitations and conclusions

Although numerous experimental studies and parametric analyses were carried out herein, there were some limitations. Since this is an early study of stainless SPSWs, no design method for stainless SPSWs was proposed. In addition, as the design methods of diagonally stiffened SPSWs with two-side connections in design standards are scarce, no applicable methods can be assessed. In the future research, we will conduct more in-depth studies on the basis of the experiments and propose a design method applicable to diagonally stiffened stainless SPSWs with two-side connections.

To promote the development of stainless steel in seismic structures and the early application of the new lateral force resisting system of stainless SPSWs in building structures, mechanical property tests under monotonic loading and cyclic loading were conducted first, and then a low cyclic loading test of 8 diagonally stiffened steel plate shear walls

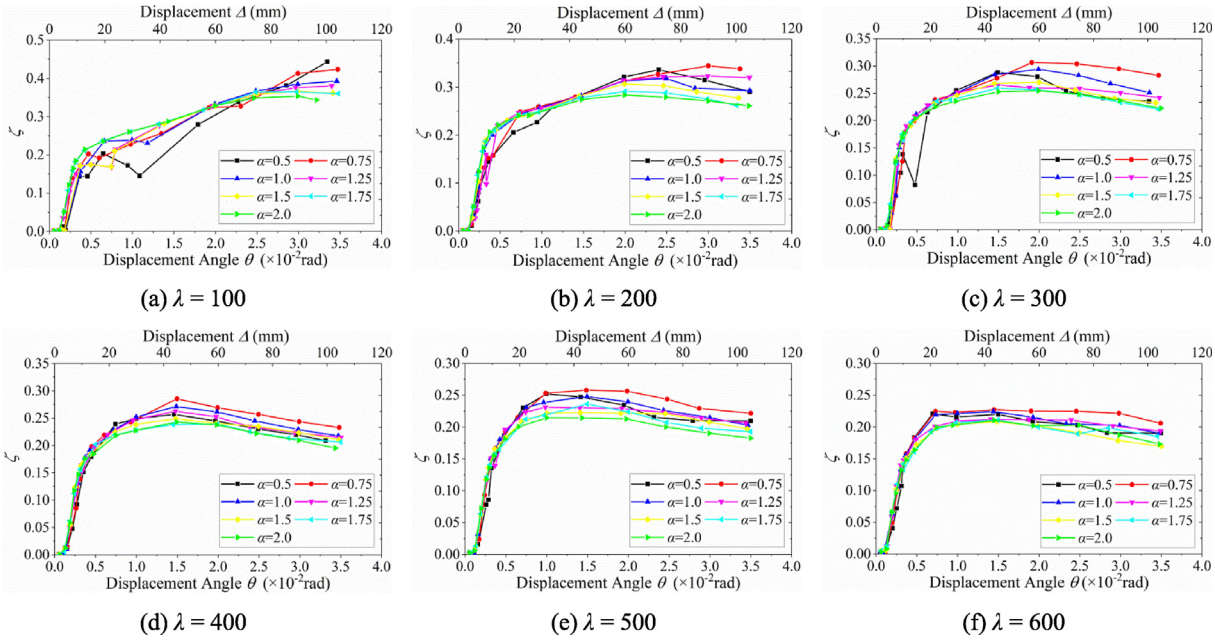

Fig. 27. ζ - θ curves of multi-parameter analysis.

was carried out. Based on the experimental study, a parametric analysis was conducted to expand the range of the investigation parameters. The main conclusions are as follows:

(1) Through the mechanical property test, S30408 austenitic stainless steel has a good energy dissipation capacity. The hysteretic behavior of stainless steel combines the characteristics of isotropic strengthening and kinematic hardening. The cyclic strengthening of the specimens is significant.

(2) In the low cyclic loading test, a transition from an elastic state to an elastic–plastic energy dissipation state is presented for all specimens. A good ductility of stainless SPSWs is presented, and stainless SPSWs more easily to form a tension field after buckling. When the displacement angle exceeds the value of 1/50, a good bearing capacity is presented. However, a poor ductility of specimens LYSW and CSW is presented, and a serious corner tearing of the steel plate occurs in the later stage of loading.

(3) For specimen LYSW, an earlier yield state occurs when subjected to low yield strength. The energy dissipation of specimen LYSW is better than that of specimens SW-1∼SW-6 and CSW in the whole loading process. Compared with Q235 steel, stainless steel has an obvious nonlinearity and can enter the energy dissipation stage more quickly. The energy dissipation of specimens SW-1∼SW-6 is better than that of specimen CSW.

(4) For specimens SW-1∼SW-3, the energy absorption and dissipation capacity become stronger, the pinch of the hysteresis curves is delayed and the initial stiffness and bearing capacity are improved as the height-thickness ratio λ increases. For specimens SW-3∼SW-5, the pinch of the hysteresis curves is more serious, the energy dissipation becomes worse and the bearing capacity is reduced as the diagonal stiffener stiffness ratio η_s decreases. The energy dissipation and bearing capacity of the specimens with the diagonal stiffener are significantly better than those without the diagonal stiffener.

(5) The aspect ratio α, height-thickness λ, stiffness ratio of periphery stiffener η_f and stiffness ratio of diagonal stiffener η_s have different effects on the hysteretic behavior of stainless SPSWs. The influence of λ is greater than that of α, indicating that λ is the key factor affecting the energy dissipation. The bearing capacity is approximately linear with α.

CRediT authorship contribution statement

Yiwen Wu: Writing – original draft, Methodology, Investigation, Conceptualization. **Shenggang Fan:** Methodology, Funding acquisition, Conceptualization. **Yang Guo:** Validation, Software, Investigation. **Shengjie Duan:** Validation, Software. **Qixun Wu:** Investigation.

Declaration of competing interest

The authors declare that they have no known competing financial interests or personal relationships that could have appeared to influence the work reported in this paper.

Data availability

Data will be made available on request.

Acknowledgments

The authors gratefully acknowledge the financial support of the National Natural Science Foundation of China (No. 51878146). The research was sponsored by Jiangsu Provincial Qing Lan Project and Jiangsu Provincial Six Talent Peaks Project, China (No. JZ-001). These financial supports are gratefully acknowledged.

References

[1] L. Gardner, The use of stainless steel in structures, Prog. Struct. Eng. Mater. 7 (2) (2005) 45–55.
[2] J. Qiu, Q.H. Zhao, C. Yu, et al., Experimental studies on cyclic behavior of corrugated steel plate shear walls, J. Struct. Eng. 144 (11) (2018) 04018200.
[3] S.J. Hilo, W.H.W. Badaruzzaman, S.A. Osman, et al., A state-of-the-art review on double-skinned composite wall systems, Thin-Walled Struct. 97 (2015) 74–100.
[4] S. Ghosh, S.B. Kharmale, Research on Steel Plate Shear Wall: Past, Present and Future. Structural Steel and Castings: Shapes and Standards, Properties and Applications, Nova Science Publishers Inc, Hauppauge, USA, 2010.
[5] P. Sharafi, M. Mortazavi, N. Usefi, et al., Lateral force resisting systems in lightweight steel frames: Recent research advances, Thin-Walled Struct. 130 (2018) 231–253.
[6] M.Z. Wang, Y.L. Guo, J.S. Zhu, et al., Sectional strength design of concrete-infilled double steel corrugated-plate walls with T-section, J. Construct. Steel Res. 160 (2019) 23–44.

[7] W. Ramberg, W.R. Osgood, Description of Stress–Strain Curves By Three Parameters, Technical Note, (902), National Advisory Committee for Aeronautics, Washington DC, 1943.
[8] H.N. Hill, Determination of Stress–Strain Relations from Offset Yield Strength Values, Technical Note, (902), National Advisory Committee for Aeronautics, Washington DC, 1943.
[9] L. Gardner, A New Approach to Stainless Steel Structural Design. London: Structures Section, Department of Civil and Environmental Engineering, Imperial College, 2002.
[10] K.J.R. Rasmussen, Full-range stress–strain curves for stainless steel alloys, J. Construct. Steel Res. 59 (1) (2003) 47–61.
[11] M. Lecce, K.J.R. Rasmussen, Distortional buckling of cold-formed stainless steel sections: Experimental investigation, J. Struct. Eng. 132 (4) (2006) 497–504.
[12] M. Lecce, K.J.R. Rasmussen, Distortional buckling of cold-formed stainless steel sections: Finite-element modeling and design, J. Struct. Eng. 132 (4) (2006) 505–514.
[13] J. Becque, K.J.R. Rasmussen, Experimental investigation of local-overall interaction buckling of stainless steel lipped channel columns, J. Construct. Steel Res. 65 (8–9) (2009) 1677–1684.
[14] J. Becque, K.J.R. Rasmussen, Experimental investigation of the interaction of local and overall buckling of stainless steel I-columns, J. Struct. Eng. 135 (11) (2009) 1340–1348.
[15] B. Rossi, J.P. Jaspart, K.J.R. Rasmussen, Combined distortional and overall flexural–torsional buckling of cold-formed stainless steel sections: Design, J. Struct. Eng. 136 (4) (2009) 361–369.
[16] B.F. Zheng, G.P. Shu, F.Z. Xie, et al., Design of cold-rolled stainless steel rectangular hollow section columns, J. Construct. Steel Res. 170 (2020) 106072.
[17] Y. Sun, A.D. Su, K. Jiang, et al., Testing, numerical modelling and design of stainless steel welded i-sections under minor-axis combined loading, Eng. Struct. 243 (2021) 112513.
[18] Y. Huang, B. Young, Experimental and numerical investigation of cold-formed lean duplex stainless steel flexural members, Thin-Walled Struct. 73 (2013) 216–228.
[19] M.F. Hassanein, N. Silvestre, Flexural behavior of lean duplex stainless steel girders with slender unstiffened webs, J. Construct. Steel Res. 85 (2013) 12–23.
[20] S. Niu, K.J.R. Rasmussen, F. Fan, Distortional–global interaction buckling of stainless steel C-beams: Part I—Experimental investigation, J. Construct. Steel Res. 96 (2014) 127–139.
[21] S. Niu, K.J.R. Rasmussen, F. Fan, Distortional–global interaction buckling of stainless steel C-beams: Part II—Numerical study and design, J. Construct. Steel Res. 96 (2014) 40–53.
[22] Y.W. Wu, S.G. Fan, L. Du, et al., Research on distortional buckling capacity of stainless steel lipped C-section beams, Thin-Walled Struct. 169 (2021) 108453.
[23] S.G. Fan, Y.W. Wu, L. Du, et al., Experimental study and numerical simulation analysis of distortional buckling capacity of stainless steel lipped C-section beams, Eng. Struct. 250 (2022) 113428.
[24] AS/NZS, Cold-Formed Stainless Steel Structures, Australian/New Zealand-Standard, AS/NZS 4673: 2001, Standards Australia, Sydney, Australia, 2001.
[25] EN 1993-1-4, Eurocode 3-Design of Steel Structures-Part 1-4: General Rules-Supplementary Rules for Stainless Steels, European Committee for Standardization, ENV 1993-1-2, CEN, Brussels, 2005.
[26] PRC National Standard, Technical Specification for Stainless Steel Structures (CECS 410:2015), China Planning Press, Bei Jing, 2015.
[27] Y.Q. Wang, T. Chang, Y.J. Shi, Experimental study on constitutive relationship in austenitic stainless steel under cyclic loading, J. Southeast Univ. (Natl. Sci. Ed.) 42 (06) (2012) 1175–1179.
[28] M. Wang, W.G. Yang, Y.Q. Wang, et al., Study on hysteretic constitutive model of austenitic stainless steel, Eng. Mech. 32 (11) (2015) 107–114.
[29] X. Chang, L. Yang, M. Wang, et al., Study on constitutive model of austenitic stainless steel and duplex stainless steel under cyclic loading, Eng. Mech. 36 (05) (2019) 137–147.
[30] T. Takahashi, Y. Takemoto, T. Takeda, et al., Portugal Lisbon, Experimental study on thin steel walls and particular bracings alternative horizontal load, in: IABSE Symposium, International Association for Bridge and Structural Engineering, 1973, pp. 185–191.
[31] M. Xue, L.W. Lu, Interaction of infilled steel shear wall panels with surrounding frame members, in: Proceedings of Structure Stability Research Council, Lehigh University, Bethlehem, 1994, pp. 339–354.
[32] M. Xue, L.W. Lu, Monotonic and cyclic behavior of infilled steel shear panels, in: Procedings of 17th Czech and Slovak International Conference on Steel Structures and Bridges, Bratislava, Slovakia, 1994, pp. 152-160.
[33] M.G. Azandariani, M. Gholhaki, M.A. Kafi, Experimental and numerical investigation of low-yield-strength (LYS) steel plate shear walls under cyclic loading, Eng. Struct. 203 (2020) 109866.
[34] M. Nakashima, Strain-hardening behavior of shear panels made of low-yield steel I: Test, J. Struct. Eng. 121 (12) (1995) 1742–1749.
[35] M. Nakashima, T. Akawaza, B. Tsuji, Strain-hardening behavior of shear panels made of low-yield steel II: Model, J. Struct. Eng. 121 (12) (1995) 1750–1757.
[36] M. Nakashima, Energy dissipation behavior of shear panels made of low yield steel, Earthq. Eng. Struct. Dyn. 23 (1994) 1299–1313.
[37] S. Torii, T. Teramoto, H. Kihara, et al., The response control design of high-rise building with low yield steel wall, in: Proceedings of Llth Word Conference on Earth, Acapulco, Mexico, 1996.
[38] PRC National Standard, Tensile Testing of Metallic Materials - Part 1: Test Methods at Room Temperature (GB/T 228.1-2010), Standards Press of China, Bei Jing, 2010.
[39] PRC National Standard, Standard for Design of Steel Structures (GB 50017-2017), China Architecture & Building Press, Bei Jing, 2017.
[40] PRC National Standard, Metallic Materials-Fatigue Testing-Axial-Strain-Controlled Method (GB/T 26077-2010), Standards Press of China, Bei Jing, 2010.
[41] Y.G. Zhu, A research for thin metal sheet fatigue test under tension-compression loading, J. Exp. Mech. (02) (2005) 241–247.
[42] L. Gardner, A New Approach To Stainless Steel Structural Design, Structures Section, Department of Civil and Environmental Engineering, Imperial College, London, 2002.
[43] Y.J. Shi, M. Wang, Y.Q. Wang, Experimental study of structural steel constitutive relationship under cyclic loading, J. Build. Mater. 15 (3) (2012) 293–300.
[44] J.L. Chaboche, Time-independent constitutive theories for cyclic plasticity, Int. J. Plast. 2 (2) (1986) 149–188.
[45] K.H. Nip, L. Gardner, C.M. Davies, et al., Extremely low cycle fatigue tests on structural carbon steel and stainless steel, J. Construct. Steel Res. 66 (1) (2009) 96–110.
[46] PRC National Standard, Specification for Seismic Test of Buildings (GB50011-2010), China Architecture & Building Press, Beijing, 2010.
[47] SAC, Protocol for Fabrication, Inspection, Testing and Documentation of Beam-Column Connection Test and Other Experimental Specimens, SAC Rep. SAC/BD-97/02, SAC Joint Venture, Sacramento, Calif, 1997.
[48] D.S. Mathew, Seismic Testing and Analytical Studies for Development of New Seismic Force Resisting Systems for Metal Buildings, University of California, San Diego, 2013.
[49] D. Wang, H.Q. Zhao, X.L. Lu, Loading protocols for quasi-static test of structural components for buildings, Sichuan Build. Sci. 40 (03) (2014) 54–59.